

STAR FORMATION HISTORIES OF NEARBY ELLIPTICAL GALAXIES. I. VOLUME LIMITED SAMPLE

JUSTIN H. HOWELL

UCO/Lick Observatory, Department of Astronomy & Astrophysics,
University of California, Santa Cruz, California 95064, USAEmail: jhhowell@ucolick.org *

Draft version January 22, 2018

ABSTRACT

This work presents high S/N spectroscopic observations of a representative sample of nearby elliptical galaxies. These observations provide a strong test of models for the formation of elliptical galaxies and their star formation histories. Combining these data with the Gonzalez (1993) data set, a volume limited sample of 45 galaxies has been defined. Results are in agreement with previous studies: the existence of the metallicity hyper-plane and the Z-plane of Trager et al. (2000) is confirmed, and the distribution is clearly due to physical variations in stellar population parameters and not measurement uncertainty. Trends between stellar population parameters and galaxy structural parameters suggest that angular momentum may determine the chemical abundance of a galaxy at a given mass.

Subject headings: galaxies: elliptical and lenticular, cD — galaxies: abundances — galaxies: stellar content — galaxies: formation — galaxies: evolution — galaxies: general

1. INTRODUCTION

Once thought to be simple old and metal-rich systems (Baade & Gaposchkin 1963), elliptical galaxies have been studied extensively over the past thirty years. A number of studies (e. g. Gonzalez 1993, hereafter G93; Rose et al. 1994; Jørgensen 1997; Tantalo, Chiosi, & Bressan 1998; Kuntschner & Davies 1998; Trager et al. 2000a; Longhetti et al. 2000; Terlevich & Forbes 2002; Caldwell, Rose, & Concannon 2003) have shown that elliptical galaxies span a wide range of ages, with a relatively small spread in metallicity $[Z/H]$. The enhancement ratio, $[\alpha/\text{Fe}]$, of Mg and nucleosynthetically related elements relative to iron peak elements is also found to be significantly greater than solar.

Trager et al. (2000b, hereafter TFWG) found that elliptical galaxies occupy a two-dimensional “metallicity hyper-plane” in the space of $[Z/H]$, $[\alpha/\text{Fe}]$, $\log t$, and $\log \sigma$, where t is the light-weighted single stellar population (SSP) equivalent age and σ is the velocity dispersion. Although cluster galaxies are older on average than field galaxies, a wide range of ages is seen in both environments (Jørgensen 1999). Gebhardt et al. (2003) suggested that a frosting of continuing star formation is necessary to explain the lack of color evolution in early type field galaxies since $z = 1$. TFWG also proposed a frosting model of star formation, as will be discussed in more detail in § 3.4. This result emphasizes the important point that the analysis of galaxy properties using SSP models does not accurately reflect the actual star formation histories of most galaxies. As TFWG and Gebhardt et al. (2003) also note, the observables do not discriminate well between different star formation histories. In multiple stellar population models, different combinations of mass fractions, ages, and metallicities can produce observationally indistinguishable galaxies.

Because the α elements are primarily produced in SN II while SN Ia produce mostly Fe, $[\alpha/\text{Fe}]$ may reflect the

duration of star formation assuming a constant, universal IMF. In high-redshift starburst, $[\alpha/\text{Fe}]$ will be high, as no SN Ia could have gone off to introduce additional Fe. In contrast, the long and continuous star formation histories typical of spiral galaxies produce $[\alpha/\text{Fe}] \sim 0$ as a result of plentiful SN Ia enrichment over billions of years. Thus abundance ratios might constrain the formation mechanism of individual galaxies. Two extreme formation mechanisms are a fast clumpy collapse model and a spiral merger model. The fast clumpy collapse model is in essence a refinement of the classical Larson (1974) monolithic collapse scenario: protogalactic gas clouds collide and merge at high redshift, forming stars rapidly as the gas dissipatively collapses to the center of the system. In a major merger of two spirals, the bulk of the total mass is already in stars formed over long timescales, while the remaining gas is metal-rich with near solar $[\alpha/\text{Fe}]$. An elliptical formed in a fast clumpy collapse would have high global $[\alpha/\text{Fe}]$ values since most stars formed from gas enriched by only a handful of SN II.

Previous spectroscopic data sets (e. g., G93, Kuntschner & Davies 1998) do not necessarily include a representative sample of elliptical galaxies in the local universe. Thus conclusions based on such data sets may reflect some unanticipated bias in sample selection rather than physical relations between structural and/or stellar population parameters of elliptical galaxies. Stellar population modeling has advanced considerably in recent years: the inclusion of nonsolar abundance ratios among α -elements as pioneered by Tripicco & Bell (1995) and Trager et al. (2000a) has been included in more recent models such as Thomas, Maraston, & Bender (2003, hereafter TMB).

This paper is organized as follows. Sample selection, observations, and data reduction are described in § 2. The data are analyzed and stellar population parameters are derived in § 3. Conclusions are presented in § 4.

2. THE DATA

2.1. Sample Selection

*now at the Infrared Processing and Analysis Center, Mail Stop 100-22, California Institute of Technology, Jet Propulsion Laboratory, Pasadena, CA 91125; jhhowell@ipac.caltech.edu

A volume-limited sample is defined, consisting of all 45 early type (E or S0) galaxies with $m - M < 32.5$ ($v < 2200 \text{ km s}^{-1}$ for $H_0 = 70 \text{ km s}^{-1} \text{ Mpc}^{-1}$), $M_B < -19.5$, $\delta > -20^\circ$, and $|b| > 15^\circ$. The galaxies were selected using the NASA/IPAC Extragalactic Database (NED). The cumulative luminosity distribution of this sample is consistent with that of a Schechter function (Schechter 1976) with the standard parameters of $M^* = -20.5$ and $\alpha = -1.07$. This suggests that the sample proposed here provides a reasonable sampling of nearby elliptical galaxies within a magnitude of M^* , and that the sample does not suffer from significant incompleteness near the faint limit. The distance measurements used in selecting this sample are from Tonry et al. (2001). The volume-limited sample is presented in Table 1. Many galaxies were previously observed by G93, and are noted as such. For newly observed galaxies we list S/N per pixel near the $\text{H}\beta$ line. Although the sample has somewhat lower S/N than the G93 sample, this has only a small effect on the total observational errors due to the typical size of calibration uncertainties; see §2.6. The 10 galaxies that were not observed are consistent with being drawn from the same population as the 35 galaxies that were observed, as judged by one-dimensional Kolmogorov-Smirnov (K-S) tests on their distribution in velocity dispersion and M_B magnitude.

2.2. Observations

The observing program used the KAST spectrograph with the 1200 lines/mm grating blazed at 5000\AA on the Lick 3 meter telescope. Observations consist of 4 – 6 25 minute exposures on a galaxy, usually with the $145''$ -long slit oriented along the galaxy's major axis, interspersed with 5 minute “blank” sky exposures on fields several arcminutes away from the target galaxy. The spectral range 4200\AA – 5600\AA was observed, with instrumental resolution of approximately 100 km/s . The velocity dispersions of the galaxies are typically $\sim 200 \text{ km/s}$. Early observing runs suffered from slightly poorer resolution as a result of suboptimal spectrograph focus. The slit width was typically $1.5''$, though in poor seeing conditions this was increased to $2''$. Spectral resolution was measured independently for each observing run to account for changes in resolution due to different slit widths or focus settings. The plate scale for the spectrograph in this configuration was $1.17\text{\AA}/\text{pixel}$ in the dispersion direction and $0.8''/\text{pixel}$ in the spatial direction.

Numerous Lick index standard star observations were made, drawing from the set of stars in common between the Lick/IDS standards of Worthey et al. (1994) and the Jones (1999) standards.

2.3. Data Reduction

Flat fields were created for each night of each observing run. The dome flat input images were averaged in the spatial direction to one dimension, and this median dispersion axis was then expanded back to the full size of the CCD. The final flat field images used in this work are the input flat fields divided by the one dimensional median for each row of the CCD. These flat field images correct for pixel-to-pixel quantum efficiency variations only. The data do not extend to red wavelengths where CCD fringing corrections become important.

Proper sky subtraction is crucial for accurately measuring line strengths in galaxies. Oversubtraction of sky flux creates spuriously large line strengths, while under-subtraction has the reverse effect. For all but the most extended galaxies, the ends of the slit provide adequate sky subtraction. This simple technique was used where applicable for the galaxies observed during or after 2002. The most extended galaxies, and those observed prior to 2002, were reduced using the offset sky spectra interspersed with the galaxy observations. The observations were not taken under photometric conditions, and the sky was found to vary unpredictably over timescales much shorter than that of a typical galaxy exposure. As a result, averaging the sky spectra taken immediately before and after each galaxy spectrum and scaling the sky spectrum by the ratio of exposure times is not sufficient for accurate sky subtraction. The proper amount of sky continuum was estimated by forcing the sky-subtracted radial brightness profile to conform as closely to an $r^{1/4}$ law (de Vaucouleurs 1948) as possible, as explained below. Burkert (1993) showed that the $r^{1/4}$ law provides an excellent fit to all elliptical galaxies between $0.1 \leq r/r_e \leq 1.5$.

First, the IRAF¹ task GEOMAP was used to rectify the galaxy spectrum such that a fixed spatial location along the slit lies at a constant y pixel coordinate. Cosmic rays and bad pixels were removed at this step. The median of the galaxy spectrum images was subtracted from each individual frame. The resulting difference frames were then divided by the median image plus a floor value equal to ten times the standard deviation at the edges of the slit. The resulting fractional deviation image was used to flag deviant pixels by interactively setting a threshold value. The flagged pixels and all neighboring pixels were masked from the input images, which were then combined to form the galaxy spectrum. Each input exposure was corrected for frame to frame variations in the background flux, putting every exposure on a common relative sky continuum scale. Specifically, the combined galaxy spectrum was subtracted from each cosmic ray corrected input spectrum. The statistics of the difference image near each edge of the slit were used to estimate a relative sky offset between the input images. The measured offsets were added or subtracted from each spectrum to place them all on a common relative sky continuum scale prior to measuring the absolute sky subtraction amount needed to fit an $r^{1/4}$ profile. Since sky intensity varies slowly with wavelength, a wavelength-independent offset was used in order to best match the sky continuum levels near the $\text{H}\beta$, Mgb , $\text{Fe}5270$, and $\text{Fe}5335$ lines. Next, the combined galaxy spectrum was collapsed along the dispersion axis in two wavelength ranges, one around the wavelength of $\text{H}\beta$ and one around the wavelengths of the Mgb , $\text{Fe}5270$, and $\text{Fe}5335$ lines, to create radial intensity profiles. An $r^{1/4}$ profile was fit to the galaxy radial profiles at intermediate radii. Finally, a constant offset was subtracted across the entire spectrum. This sky continuum level was determined to be that offset which results in the best fit to a de Vaucouleurs profile extending to

¹ IRAF is distributed by the National Optical Astronomy Observatories, which are operated by the Association of Universities for Research in Astronomy, Inc., under cooperative agreement with the National Science Foundation.

large radii. In practice little difference was found between the best fit offset in the two wavelength ranges used to produce radial intensity profiles.

Extraction and dispersion correction of the spectra used standard IRAF packages. The input spectra to these tasks incorporate the relative and absolute sky continuum adjustments described above, and have been median combined with cosmic ray rejection as above, but have not been rectified. Instead, the extraction procedure traces the object spectrum across the CCD. The galaxy spectra were extracted in apertures extending to $r_e/8$ from the galaxy center, as per G93. Effective radii were taken from Faber et al. (1989). Galaxies were dispersion corrected using lamp spectra taken immediately before or after the galaxy observations, at the same telescope position. These lamp spectra were extracted using the same trace as the galaxy spectra. A high-order polynomial (typically fifth order) was fit to the ~ 30 lamp lines, and this dispersion correction was then applied to the galaxy spectrum. Typical wavelength calibration uncertainties are $\sim 0.10\text{\AA}$.

2.4. Lick Indices

Line widths of the Lick indices defined in Trager et al. (1998) and Worthey & Ottaviani (1997) were calculated using a version of the `bwid` program, provided by R. M. Rich (Rich 1998). As `bwid` is not an IRAF procedure, the data were read out into ascii files for input. Test spectra from Guy Worthey's web page² were used to confirm the accuracy of `bwid`. Two sets of Lick/IDS indices were measured. The primary set of indices consists of $\text{H}\beta$, $\text{Mg}\,b$, $\text{Fe}5270$, and $\text{Fe}5335$, while $\text{H}\gamma_F$, $\text{Ca}4227$, $\text{G}4300$, $\text{Fe}4383$, $\text{Ca}4455$, $\text{Fe}4531$, C_24668 , $\text{Fe}5015$, and $\text{Fe}5406$ form the secondary set of indices (Table 2). The two sets are distinguished by both scientific and practical considerations. The primary set comprises the indices in common use in previous observational studies (e. g. Trager et al. 2000a). Furthermore, the spectral range of the models of Schiavon (2005) allow for sophisticated error simulations of the primary indices, while simpler error estimates must be used for many of the secondary indices; see § 2.5 for details.

Several corrections must be applied before equivalent widths can be measured. First, the galaxy sample must be adjusted to a common radial velocity, $v = 0$. The extensive model library of Schiavon (2005) was used to provide an empirical Doppler correction. The galaxy spectra were cross correlated with an old, metal rich model spectrum, and the resulting velocity was used in the Doppler correction.

Next, the galaxy sample was corrected to zero velocity dispersion. The following procedure was used. The model spectra were rebinned to match the Doppler-corrected galaxy spectrum. An analytic continuum function was fit to the galaxy and each model spectrum. The model spectra were divided by their respective continuum functions, then multiplied by the galaxy continuum function to match the shape of the observed galaxy spectrum. A copy of each model spectrum was then smoothed to the velocity dispersion of the galaxy using the σ measurements from Faber et al. (1989). A least-squares fit was performed to select the appropriate model for each

galaxy. The fit was performed within a spectral region surrounding the $\text{Mg}\,b$, $\text{Fe}5270$, and $\text{Fe}5335$ lines: 5140–5370 \AA . To empirically refine the galaxy's velocity dispersion, the $\sigma = 0$ version of the best fitting model spectrum was used as a template for the `Pixel` code from van der Marel (1994). The resulting σ was then corrected for the different instrumental resolution of the galaxy and model spectra. The best fit model was then rebinned to a logarithmic wavelength scale and gaussian smoothed to the measured velocity dispersion of the galaxy, again taking the intrinsic resolution of the model spectrum into account. After transforming back to a linear wavelength scale, line widths were measured in the $\sigma = 0$ model spectrum smoothed to Lick/IDS resolution and the model spectrum smoothed to the galaxy's velocity dispersion and then to the Lick/IDS resolution. The ratio of the two measurements is the correction factor applied to the corresponding equivalent width measured from the galaxy spectrum. For a few indices ($\text{Fe}4383$, $\text{Ca}4455$, $\text{Fe}4531$, and C_24668) no model spectra were available covering the appropriate wavelengths; for these indices σ -corrections were calculated from Trager et al. (1998).

As indicated above, it is necessary to degrade spectra to the resolution of the Lick Image Dissector Scanner instrument which was used to make the stellar observations upon which the Lick/IDS system is based. The resolution function of this instrument is taken from Worthey & Ottaviani (1997). Since the resolution varies strongly with wavelength at the blue end, smoothing was done piecewise in 100 \AA increments in that part of the spectrum, while a constant value was appropriate for the red end.

An emission correction was required to accurately measure the $\text{H}\beta$, $\text{H}\gamma_F$, and $\text{Fe}5015$ indices. The $[\text{OIII}]\lambda 5007$ line was used to estimate the amount of $\text{H}\beta$ emission (Trager et al. 2000a). Since $[\text{OIII}]\lambda 5007$ is adjacent to the $\text{Fe}5015$ line, it is impossible to accurately determine the continuum level. Instead, model spectra were used. The best fitting model was subtracted from the galaxy spectrum, and the intensity of $[\text{OIII}]\lambda 5007$ was measured on the difference spectrum. This line was measured by hand using the IRAF task `SPLIT`. The result was then converted to equivalent width using an estimate of the intensity level of the galaxy spectrum near $[\text{OIII}]\lambda 5007$. The $[\text{OIII}]$ emission was converted to an $\text{H}\beta$ correction using Equation 2 of Trager et al. (2000a). $\text{H}\gamma_F$ and $\text{Fe}5015$ were corrected as described in Kuntschner et al. (2002), with correction factors of $0.36 \times [\text{OIII}]\lambda 5007$ and $0.61 \times [\text{OIII}]\lambda 5007$ respectively. In NGC 1052 $\text{H}\beta$ appears only in emission. NGC 3226, with the next strongest $[\text{OIII}]\lambda 5007$ line, also shows $\text{H}\beta$ emission within the absorption line, while all other galaxies show at most a slight distortion in the shape of the $\text{H}\beta$ absorption.

Lick index standard stars were used to calibrate the output line widths. The reduction procedure for standard star observations is a simplified version of that described above for the galaxy observations. A typical standard star is observed in five consecutive exposures of a few seconds integration time. After flat fielding and dark subtraction, the individual frames are median combined and then extracted. Sky subtraction is performed via a linear fit between two sky regions near the star on the

² <http://astro.wsu.edu/worthey/html/system.html>

slit. The stellar spectrum is extracted in a user-defined aperture extending to the points at which the PSF disappears into the sky background. This aperture is traced across the CCD as above. As with the galaxy spectra, the accompanying calibration lamp spectra are extracted in the exact same aperture as the stellar spectrum. After dispersion calibration, the smoothing described above is applied. Radial velocities are determined empirically by cross correlation, in this case using the Jones spectra of the same star as templates. The standard star spectrum is read out into an ascii file, and line widths are measured by `bwid`. Corrections for each of the Lick indices are derived by comparing the observed stellar line widths for each observing run to the standard values. These calibration offsets are not constant from run to run, particularly for the Fe5335 index.

The data from this project are not flux-calibrated, while the Lick/IDS system was calibrated to a quartz lamp response curve. This mismatch is absorbed into the calibration corrections. The standard stars and galaxy spectra were observed with the same CCD, grating and grating tilt, and are thus on a common system. Errors in the mean for the IDS calibration to the primary indices are 0.04–0.06Å, though run to run variations are often much larger. Fully corrected measurements for each index, including estimates of the total error (§ 2.7) in each index, are presented in Table 2.

Figure 1 shows the measurements for each index plotted against the galaxy’s velocity dispersion. The $Mg - \sigma$ relation (Bender et al. 1993) is clearly evident, with Ca4227 and C₂4668 following the same trend. The iron indices show similar behavior but with greater scatter, forming a mass-metallicity relation. The two Balmer indices both follow the well-known trend that larger galaxies tend to have smaller values than smaller galaxies. The five galaxies with large ($> 0.5\text{Å}$) [OIII] $\lambda 5007$ emission are omitted from subsequent analysis due to their large uncertainties.

2.5. Error Simulations

Empirical error simulations were performed as follows using the model spectra described previously. The model spectrum used in the velocity dispersion correction forms the basis for the error simulations for the corresponding galaxy.

Several potential sources of random error were simulated. Poisson noise was modeled by adding the quadrature sum of the galaxy poisson noise and sky spectrum poisson noise to the model spectrum. The poisson errors were derived from the raw spectra (flat fielded only, no dark or sky subtraction), in units of electrons rather than ADU.

Error in the subtraction of the night sky lines was estimated as follows. The pixel value of the sky lines was multiplied by a small factor f and added in quadrature to the above poisson error. The value of f was chosen such that the simulated spectrum best matched the true galaxy spectrum. Sky line subtraction error proved to be unimportant: $f = 0$ provides a good match to the galaxy spectra.

To investigate the possibility of flat fielding error, a noise floor was introduced into the error calculations. This floor was simply added in quadrature to the poisson error, and the value of the noise floor was chosen so that

the simulated spectrum best matched the galaxy spectrum. As with sky line subtraction noise, flat fielding noise proved to be unimportant, and a noise floor of zero was used.

Two other sources of error are directly measured and included in the simulations. The uncertainty in the dispersion solution is calculated by IRAF, and the error in sky continuum subtraction is easily estimated. These errors are included in the simulations, the first as a random shift in the wavelength scale and the second as a random shift in the continuum level of the model spectrum. Sky subtraction error may be underestimated by this method, particularly at the blue end of the spectrum, far from the wavelength range in which the sky subtraction measurements were made.

Error simulations were performed in groups of 1000 to provide accurate statistics. Each simulation spectrum was measured by `bwid` in exactly the same way that actual galaxy spectra were measured. Three galaxies were used as the basis for these simulations: NGC 3115, the galaxy with the highest S/N in the sample, NGC 1209, a galaxy with S/N typical for the bulk of the galaxy sample, and NGC 4168, a galaxy with relatively poor S/N .

2.6. Calibration Uncertainty

The uncertainty in the calibration to the Lick/IDS system deserves particular attention because for many indices this is the dominant source of error. The observed standard star primary index measurements are compared to the Lick/IDS values in Figs. 2 and 4. The former shows that a constant calibration offset can correct the observations onto the standard system — no first-order term in index strength is needed for the calibration. Fig. 4 highlights the run-to-run variations in the necessary calibration offset. These offsets are calculated separately for each run, except for 2003 January 2 (Run 4) which was incorporated in the 2002 November (Run 3) run calibration due to the limited data obtained that night. The calibrated standard star index measurements are compared to the Lick/IDS values in Figs. 3 and 5, plotting the difference between calibrated and standard values against the standard value and the run number, respectively. The external error in calibrating the data to the Lick/IDS system is taken to be the error in the mean calibration offset for each run. These external errors are shown at the right of Figs. 4 and 5; the error bars are omitted in Figs. 2 and 3 for clarity.

The repeated observations of a subset of standard stars in several observing runs allows the internal calibration error to be measured. Fig. 6 shows these repeat observations for each run. Instead of plotting the difference between the calibrated and standard index values for each star as above, in this figure the difference between calibrated individual observations and the average of all observations of that star is shown.

Though not often listed, it is straightforward to calculate the uncertainty within the Lick/IDS system in any given observing run. Worthey et al. (1994) lists the typical error for an individual IDS measurement of each Lick index. Since each standard star was given equal weight in the calibration to the Lick/IDS system, the IDS internal error was calculated as the average of the errors in the individual stars, weighted by the number of IDS observations.

The calibration to the Lick/IDS system is shown in Fig. 7. The calibrated standard star observations from this work are in good agreement with both the Lick/IDS system and standard star observations from G93.

2.7. Additional Errors

Several sources of error not included in the simulations can also affect the equivalent width measurements to varying degrees. These include incorrect radial velocities, velocity dispersions, emission correction, and calibration error, as well as possible problems with the adopted data reduction procedures.

Preliminary data reduction demonstrated that published radial velocities for the galaxies or standard stars do not necessarily agree with the observed spectra. The mismatches could be over 100 km/s in magnitude, with correspondingly large effects on the equivalent width measurements. This source of systematic error is avoided through the use of our empirical radial velocity measurements, as described above. Though the preliminary reductions did not show any similar problem with published velocity dispersions, empirical measurements were again chosen for the same reason.

Velocity dispersion corrections are known to be very index-dependent (Trager et al. 1998). The fitting functions from that work were used to translate a conservative error estimate $\sigma_\sigma \approx 10$ km/s into index errors. These errors proved to be negligible for $H\beta$ and Mgb . The actual errors in σ are estimated to be $\sim 3\text{--}5$ km/s by the Pixfit code. The uncertainty in the measured velocity dispersion is the quadrature sum of the internal error measured by Pixfit with an estimate of the additional uncertainty due to template mismatch. The latter quantity was estimated to be ~ 3 km/s based on comparing the measured velocity dispersions using several model spectra which fit the data nearly as well as the best fit spectrum. The measured velocity dispersions can easily be compared with data in the literature, as shown in Fig. 8. The mean offset is 3 km/s with an RMS scatter of 11 km/s.

The emission correction for $H\beta$, $H\gamma$, and $Fe5015$ can drastically increase the error for those galaxies for which the correction is large. The error in $[OIII]\lambda 5007$ emission was estimated by measuring the emission line in the difference spectrum (see above) using several different continuum levels. The average difference between these alternate continuum level equivalent width measurements and the zero continuum equivalent width measurement (which assumes a perfect match) was achieved between the continuum levels of the model and observed spectra) was taken to be the uncertainty in the $[OIII]\lambda 5007$ measurement. For many galaxies with little or no $[OIII]\lambda 5007$ emission, this uncertainty is negligible, while for the galaxies with the largest $[OIII]\lambda 5007$ emission lines the uncertainty is so large as to render the emission corrections extremely suspect. The five galaxies with $[OIII]\lambda 5007$ emission greater than 0.5 Å equivalent width have been omitted from subsequent analysis of the volume-limited sample due to the large uncertainties.

An important potential source of systematic error is the method of background subtraction. Preliminary reductions tested two different techniques. The method using sky exposures is described above. A simpler technique of simply subtracting a linear interpolation of the

background between two user-defined regions near the edge of the slit was also tested. The latter technique is the most common in the literature (G93 long slit observations, Beuing et al. 2002), though the possibility of age and abundance gradients makes it dubious for galaxies of large angular size. For most galaxies in this study, the slit edges provide adequate sky subtraction. Reducing the same galaxy using both sky subtraction methods results in final index measurements which differ by much less than the total uncertainties. This check also indicates that the technique described above using the sky exposures does not introduce significant wavelength-dependent biases into the spectrum at the blue end.

In addition to sky continuum subtraction, the bright $Hg4358$ night sky line contaminates the $G4300$ and $H\gamma F$ indices. The uncertainties of those indices are undoubtedly larger than estimated, and the uncertainties are likely to vary with galaxy redshift depending on whether the sky line falls in the index bandpass or a sideband.

If the input images have non-negligible subpixel offsets from one another in the dispersion direction, it is possible that the effective instrumental resolution could be artificially degraded when the images are combined into the final two dimensional galaxy spectrum. To test for this, one galaxy (NGC 1209) was re-reduced in a different manner following sky subtraction. Each input frame was reduced separately. Wavelength calibration was performed on the two dimensional images using standard techniques (IDENTIFY, REIDENTIFY, FITCOORDS, and TRANSFORM in IRAF's LONGSLIT package). The $r_e/8$ aperture on each was traced and extracted, then doppler corrected and smoothed to Lick/IDS resolution. The average index values showed no significant difference from those derived using the previous data reduction technique. Pixfit measured velocity dispersions less than 5 km/s smaller than those measured on the combined extraction previously. We conclude that there is little loss of effective instrumental resolution from combining input images.

Since NGC 1209 was also used in the error simulations, the alternate reduction procedure above also provides an independent test of the estimated errors for each index. The alternate technique should measure only the random poisson errors between the spectra. Thus *a priori* one expects smaller error bars than those estimated from the simulations which include several possible sources of systematic error as well. The error comparison confirmed this expectation, except for Mgb where the two error estimates were equal.

The final error bars adopted for the primary indices for each galaxy are a quadrature sum of the errors from the error simulation appropriate for that galaxy's S/N , the errors in σ -correction and emission correction, and the internal and external calibration errors. Table 3 lists typical values for each of these quantities, as well as the uncertainty within the IDS system for a typical observing run. Errors for the secondary indices are taken from the scatter in the measurements of each index in the NGC 1209 individual frames, added in quadrature as above with the σ -correction, emission correction, and IDS calibration errors. Since the calibration error is a large contribution to many of these index errors, the results should be reasonably accurate even for galaxies of significantly lower S/N than NGC 1209.

As a final consistency check, index measurements from this study are compared with measurements of the same galaxies from G93 and Denicoló et al. (2005) in Fig. 9. An equivalent comparison between G93 and Denicoló et al. is shown in Fig. 10. The measurements from this study are found to be in good agreement with G93. The Denicoló et al. sample is found to have larger error bars and systematic offsets in each measured quantity compared to both G93 and this study. Although crucial as an intermediate step in establishing the consistency between the latter two data sets, the Denicoló et al. sample will not be included in the discussion in § 3.

3. ANALYSIS

3.1. Stellar Population Parameters

The Balmer indices ($H\beta$, $H\gamma_F$, and $H\delta_F$) are the most commonly used age indicators in stellar population analysis. The data in this study do not include the $H\delta_F$ index, but both $H\beta$ and $H\gamma_F$ have been measured. Kuntschner et al. (2002) presents a detailed discussion of the relative merits of each index (see also Caldwell et al. (2003) for a discussion of the $H\beta$ index compared to higher order Balmer line ratios). Briefly, $H\beta$ suffers from nearly twice the contamination of nebular emission lines (if present) filling in the stellar absorption. $H\gamma_F$ also offers increased dynamic range between young and old stellar population models. Offsetting this, $H\beta$ measurements normally achieve higher S/N due to the combination of the red colors of early-type galaxies and the typical sensitivity curves of CCDs and spectrograph optics diminishing at bluer wavelengths. Both indices can suffer from metal line contamination in the continuum measurement. Strader & Brodie (2004) showed that $H\beta$ suffers from additional variance caused by weak Fe I lines in the wavelength range of the index. As a result, ages based on $H\beta$ can be less reliable than those based on $H\gamma$ or $H\delta$, as seen in the extragalactic globular cluster study of Puzia (2003) (see also Howell et al. (2004)). However, $H\gamma_F$ can suffer from CH contamination and as noted in § 2.7 is often affected by a bright night sky line, neither of which are issues for $H\beta$. Pragmatically, $H\beta$ is the age indicator of choice for this study, as the G93 data set does not include measurements of $H\gamma$ or $H\delta$. A comparison of age measurements using $H\beta$ and $H\gamma_F$ for the galaxies from this study will be presented below (§ 3.2).

The fully calibrated and corrected equivalent widths for the galaxy sample are presented in Fig. 11, plotted on the $H\beta$ – $[\text{MgFe}]'$ plane. The age–metallicity grid of the TMB models is also plotted. The composite index $[\text{MgFe}]'$ was defined in TMB as an overall (i.e. $[\text{Z}/\text{H}]$) metallicity index that should be independent of $[\alpha/\text{Fe}]$ based on their calculations using the response functions of Tripicco & Bell (1995). Members of the volume-limited sample observed by G93 are also plotted. The SSP age and metallicity for each galaxy was measured by linear interpolation among the TMB models in each quantity.

The α -enhancement for each galaxy was measured using the TMB models. Since age does not strongly affect the location of lines of constant $[\alpha/\text{Fe}]$ in the Mgb – $\langle \text{Fe} \rangle$ plane, each galaxy need not be compared individually to the model of precisely matching age as measured from Fig. 11. The 3 Gyr model was used to measure $[\alpha/\text{Fe}]$ for each galaxy, and an age correction was then applied.

This age correction was calculated by linearly interpolating the offsets perpendicular to isoenhancement lines between models with ages of 3, 8, and 15 Gyr. The galaxy sample and the models are plotted in Fig. 12.

Errors in age and metallicity are derived from the index errors in $H\beta$ and $[\text{MgFe}]'$. The extrema of the error ellipse defined by $\sigma_{H\beta}$ and $\sigma_{[\text{MgFe}]'}$ in the directions perpendicular to isochrone and isometallicity lines were used to define σ_t and σ_Z respectively. These stellar population uncertainties are highly correlated. Errors introduced by the interpolation of the TMB model are estimated to be 0.05–0.1 Gyr (depending on age) and ≤ 0.01 dex in $[\text{Z}/\text{H}]$, in each case negligible compared to the errors derived from the index uncertainties.

The error in α -enhancement is derived in a similar fashion, with the added complication of including σ_t . The extrema of the $\sigma_{\text{Mgb}}-\sigma_{\langle \text{Fe} \rangle}$ error ellipse in the direction perpendicular to the isoenhancement lines are combined with ages of $t \pm \sigma_t$ in the sense that maximizes the resulting spread in measured $[\alpha/\text{Fe}]$.

Parameter values and associated errors are presented in Table 4. Galaxies from G93 are listed in the bottom portion of the table. For consistency, the index measurements from G93 were used to determine stellar population parameters from TMB rather than using the parameters from Trager et al. (2000a).

3.2. Model Uncertainties

The choice of model can strongly affect the values of the physical quantities one derives from spectral line index measurements. The importance of measuring the G93 galaxies with respect to the TMB models is clearly shown in Figure 13. The TMB models result in higher $[\alpha/\text{Fe}]$ (by an average of 0.06 dex) and $[\text{Z}/\text{H}]$ (by an average of 0.1 dex) than the Worthey models used by TFWG. This suggests that the earlier models yield the correct Fe abundance, but underestimate the α -elements and thus also $[\text{Z}/\text{H}]$.

The $H\gamma$ index is measured in the data from this work, and a comparison between the age estimates using $H\beta$ and $H\gamma$ can be made as a check on the extent to which the choice of Balmer index affects the resulting age estimates. Within this Balmer line comparison, it is also instructive to compare the effect of using different SSP models. The models of Schiavon (2005) are used for this purpose. First, the Balmer index measurements are compared with one another in Fig. 14. With the exception of four outliers, the two indices are tightly correlated as expected. Figures 15 & 16 show the galaxies presented in this study plotted on the $H\beta$ vs. $\langle \text{Fe} \rangle$ and $H\gamma_F$ vs. $\langle \text{Fe} \rangle$ planes respectively. The TMB and Schiavon model grids are plotted on the former, and the Thomas, Maraston, & Korn (2004) and Schiavon model grids are plotted on the latter. All models have $[\alpha/\text{Fe}] = 0$. Ages derived using each set of models are plotted against each other in Fig. 17. As is apparent from a visual inspection of the grids, an age offset of several Gyr exists between the Thomas et al. and Schiavon model grids, in the sense of the Thomas et al. models yielding (on average) younger ages on $H\beta$ grids and older ages on $H\gamma_F$ grids compared to the Schiavon models. The outliers in Fig. 14 remain outliers in Fig. 17 using either set of models. The quantitative difference between age estimates from the two sets of models suggests that the choice of SSP model is

more important than the choice of Balmer index when attempting to measure ages by this method. Since the two sets of models each produce consistent age measurements for some range of ages (Thomas et al. models are consistent for old galaxies; Schiavon models are consistent for young galaxies), for the purposes of this study there is no clear reason to prefer one to the other. Therefore the choice to use the TMB models and measure SSP parameters on model grids with $H\beta$ as the age-sensitive index does not introduce any additional systematic error due to choice of models or Balmer index. Note that the above comparisons do indicate the presence of systematic errors arising from both sources, however the same would be true regardless of the models or Balmer index selected. Also, an inconsistency between ages derived using $H\beta$ and $H\gamma$ does not necessarily imply that the SSP model being used is incorrect in some way. As noted in § 1, single stellar populations are a necessary simplifying assumption, but galaxies in general will have stellar populations of varying ages and metallicities. Such a composite stellar population can easily yield different ages derived using $H\gamma$ as the age sensitive index compared to using $H\beta$ as the age sensitive index.

3.3. Multiple Stellar Population Analysis

Current stellar population analysis techniques rely on the single stellar population (SSP) assumption, that a single age, metallicity, and α -element abundance ratio can characterize the stellar population of a galaxy. More realistic stellar population models can be constructed, however there is no widely applicable method to fully constrain the problem — even in the simplest case of assuming two starbursts instead of one, the number of free parameters is more than double that of the SSP case (two ages, two $[Z/H]$, two $[\alpha/Fe]$, and the mass ratio between the two bursts). Allowing for a larger number of bursts or continuous star formation further underconstrains the problem. In a few galaxies, SSP observations of their globular cluster (GC) populations (for which the SSP assumption is correct rather than a means to obtain a luminosity-weighted average) may allow two-burst multiple stellar population models. Almost all elliptical galaxies contain at least two populations of GCs, as seen in bimodal color distributions (e. g. Zepf & Ashman 1993). Measurements of these two GC populations allow the two sets of stellar population parameters for a two-burst galaxy model to be set in a consistent way. Howell et al. (2004) showed that this does not always work; if the youngest GC population is coeval with the SSP age of the galaxy the resulting mass ratio between the two starbursts will necessarily be strongly weighted towards the younger burst. As shown in Trager et al. (2000b), for example, although a small mass fraction of young stars is sufficient to change the measured SSP age by several Gyr, mass fractions of 50% or more are required to produce SSP ages consistent with that of the young population itself. Such large burst fractions are contrary to most expectations for galaxy formation.

The GC populations of a few galaxies in the volume-limited sample have been studied spectroscopically. With stellar population information for two GC populations, the age, $[Z/H]$, and $[\alpha/Fe]$ for each burst can be estimated rather than being free parameters. In practice, $[\alpha/Fe]$ can be ignored as the best available models

for multiple stellar population analysis remain those of Worthey (1994) via Worthey's Dial-a-Galaxy web page³, which do not account for non-solar abundance ratios.

The requisite data exist for four galaxies: NGC 3115, NGC 3610, NGC 4365, and NGC 5846. NGC 3610 is discussed in detail in Howell et al. (2004). Using IR photometry, Puzia et al. (2002) found candidate intermediate-age GCs associated with NGC 4365. These candidates were seemingly confirmed by Larsen et al. (2003) finding a young and metal rich GC population with an age between 2–5 Gyr and approximately solar metallicity. However, Brodie et al. (2005) found that based on all Balmer lines the GC population was coeval within the errors, with an age > 10 Gyr. The data from Larsen et al. (2003) were biased by low S/N in the sense that some but not all of the intermediate age candidates from Puzia et al. (2002) appeared young using only the $H\beta$ index. Since the GC population is older than the SSP age of the galaxy, no viable two burst model can be constructed using the GC populations to constrain the bursts. NGC 3115 appears to be a similar case, with old GCs (Kuntschner et al. 2002) around an intermediate age galaxy. Trager et al. (1998) suggest that the galaxy itself is also old, however the NGC 3115 data presented here are of exemplary S/N with negligible emission correction, and conclusively indicate an age between 4–7 Gyr depending on whether $H\beta$ or $H\gamma$ is used as the age-sensitive index. The aperture used in this work is larger than that of the data analyzed in Trager et al. (1998), and Bassin & Bonatto (2003) showed that the contribution of a young stellar population increases with radius on the scale covered by aperture used here. The discrepancy between the measurement presented here and that of Trager et al. (1998) is therefore explained by differing stellar populations in the apertures used in each study. NGC 5846 (Puzia et al. 2004) has uniformly old GC populations at a range of metallicities. Since the galaxy has an old SSP age (Table 4), the SSP assumption appears to be a reasonable approximation to the star formation histories of this galaxy.

3.4. Correlations Between SSP Parameters

In Fig. 18 all galaxies in the volume-limited sample observed thus far are plotted on the metallicity “hyperplane” of TFWG. Error ellipses in the hyper-plane projections were calculated from the errors in the individual indices. Index errors were treated as independent quantities, as sky subtraction error is negligible at the centers of galaxies. Monte Carlo simulations were run propagating index error realizations for a particular galaxy into physical parameters and thence to the principal component axes of the hyper-plane. The RMS scatter about the major and minor axes of the Monte Carlo distribution in the hyper-plane was used for the major and minor axis lengths of the 1σ error ellipses. The actual error distribution is not quite symmetrical: as one expects from looking at the model grids, a fixed level of index scatter leads to unequal parameter scatter in the young and metal-rich directions compared to the old and metal-poor directions. The hyper-plane is clearly due to physical variations between galaxies, not measurement error or bias. The volume-limited and G93 samples have

³ http://astro.wsu.edu/worthey/dial/dial_a_model.html

similar distributions within the hyper-plane.

The Z -plane from TFWG (Fig. 19) provides an intriguing challenge to theories of galaxy formation. This projection shows that a linear relationship exists between $[Z/H]$, $\log \sigma$, and $\log t$. TFWG showed that no other galaxy parameters significantly affected this fit. The fit from TFWG is plotted; however a slight offset would better fit the data presented here. This is the result of using the TMB SSP models instead of the Worthey models used by TFWG; recall that Fig. 13 showed a constant offset between the two sets of models in the $[Z/H]$ measurements. This offset in $[Z/H]$ requires a corresponding offset in the Z -plane fit. As discussed in detail in TFWG, single burst models cannot plausibly produce a Z -plane relation — a linear relation at the present epoch would be noticeably curved at past and future times, as old objects change less in $\log t$ than young objects. TFWG showed that a two (or several) burst “frosting” model can in principle maintain the Z -plane over time. Such frosting populations most plausibly form from gas within the galaxy and enriched by previous star-formation events; it is unlikely that accreted gas or a merger event would have the appropriate metallicity to keep the galaxy on the Z -plane. However, the young and metal-rich end of the Z -plane tends to be populated by likely merger remnants such as NGC 3610, the most extreme such galaxy in the volume-limited sample. As shown in Fig. 19, NGC 3610 lies directly on the Z -plane, as do other similar galaxies from the G93 sample which are also believed to be merger remnants (TFWG).

The volume-limited sample is compared with the G93 sample in all four principal component axes, as well as position along the edge-on projection of the Z -plane. K-S tests indicate that the volume-limited sample is consistent with being drawn from the same distribution as the G93 sample in all five dimensions. This confirms that the G93 galaxies are representative of the early-type galaxy population in the local universe.

3.5. Correlations with Other Parameters

Having derived stellar population parameters for the galaxies in the volume-limited sample, as well as rederiving the stellar population parameters for the G93 sample using the same models, we now turn our attention to other physical parameters of these galaxies. Figure 20 shows the stellar population parameters age, $[Z/H]$, and $[\alpha/\text{Fe}]$ plotted against three structural parameters, σ , M_B , and r_e , as well as the anisotropy parameter $(v/\sigma)_*$ (Bender, Burstein, & Faber 1992; Faber et al. 1997), the core profile slope γ (Lauer et al. 2005), and the $B - V$ color gradient (Idiart, Michard & de Freitas Pacheco 2002). These quantities are listed in Table 5. Note that the relatively small magnitude range covered by this sample limits the ability to investigate correlations involving luminosity or quantities closely tied to luminosity. For each pair of parameters plotted against each other, the correlation statistic was calculated, excluding those galaxies with large emission corrections. The Kendall’s τ rank correlation test was used to identify correlations which were not significant. Unfortunately the Kendall’s τ test can only rule out correlations; it cannot identify which correlations are significant, as demonstrated in trials where it found nominally significant correlations between NGC number and various physical parameters.

The Spearman rank correlation test was found to have similar behavior. Thus a correlation is judged to be significant if it is not ruled out by the Kendall’s τ test and the absolute value of the correlation statistic is greater than a threshold value, arbitrarily chosen to be 0.3. By these criteria, significant correlations are found between σ and both age and $[\alpha/\text{Fe}]$; and between $\log r_e$ and age. The relation between $[\alpha/\text{Fe}]$ and σ is a representation of the well-known $\text{Mg}-\sigma$ relation. The other two relations indicate that the smallest galaxies, measured either by radius or mass, are younger than larger galaxies, as expected from the “downsizing” galaxy formation scheme of Cowie et al. (1996). This result is in agreement with the more comprehensive study of low velocity dispersion galaxies by Caldwell et al. (2003).

Early-type galaxies lie on planes in two different parameter spaces, the Fundamental Plane and the metallicity hyper-plane. The existence of a mapping from one plane to the other would imply a relation connecting the size and brightness of a galaxy to its age and chemical composition. To search for such a mapping, the κ -space parameterization of the Fundamental Plane was used (Bender et al. 1992). The two planes are shown in Fig. 21. The IRAF task GEOMAP found no combination of scale factors, rotations, and translations that can map the $\kappa_1-\kappa_2$ face-on projection of the Fundamental Plane into the PC1-PC2 face-on projection of the metallicity hyperplane. The best fit resulted in average offset distances of 0.15 in the PC1-PC2 plane (average offset of 0.07 in the PC1 axis and 0.11 in the PC2 axis individually). The largest offsets occurred for the most extreme galaxies in one or both axes, up to a difference of 0.52 in PC2 for one galaxy. As a result, the transformed Fundamental Plane distribution covers a smaller portion of the PC1-PC2 plane than the metallicity hyper-plane. The transformed Fundamental Plane distribution is found to be consistent with the metallicity hyper-plane by K-S tests, though the consistency is marginal (K-S probability of 8%) on the PC2 axis. Also, as previously noted, the sample presented here covers a relatively small range of luminosity and therefore may lack leverage to reveal important details within these parameter spaces.

The stellar brightness profiles of 27 of the galaxies in both the volume-limited sample and the G93 sample have been studied with HST (Faber et al. 1997; Lauer et al. 2005). Figure 20 showed no significant correlations between the brightness profile slope γ and any stellar population parameter, though this test was restricted to the subset of the volume-limited sample for which HST surface brightness profiles are available. Combining all available galaxies, including G93 galaxies not included in the volume-limited sample, the distribution of σ , age, $[Z/H]$, and $[\alpha/\text{Fe}]$ among both core and power-law galaxies was examined using K-S tests. The two classes of galaxies are consistent with having the same distribution of age and metallicity (probabilities 0.087 and 0.82, respectively), while core galaxies have significantly higher velocity dispersions and $[\alpha/\text{Fe}]$ values than power-law galaxies (probabilities of 0.019 and 0.036, respectively). This is as expected given the result of (Faber et al. 1997) that the most luminous galaxies all have core profiles, while all galaxies below a certain luminosity threshold ($M_V > -20.5$) have power-law profiles. To further explore the meaning of these relations, the distribution

of stellar population parameters between galaxies with boxy or disky isophotes was examined. Since Faber et al. (1997) found a strong correlation between galaxies with disky isophotes and power law core profiles, the expectation is that the disky galaxies will have lower $[\alpha/\text{Fe}]$ and σ measurements. Isophotal shape measurements for 15 galaxies are listed in Idiart et al. (2002), and the a_4/a parameter from Faber et al. (1997) was used to determine the shapes of an additional 13 galaxies. Boxy and disky galaxies are consistent with being drawn from the same distribution in σ , age, and $[\text{Z}/\text{H}]$ (probabilities of 0.43, 0.23, and 0.75, respectively), while disky systems have significantly smaller $[\alpha/\text{Fe}]$ than boxy systems as expected (probability of 0.048).

Carollo et al. (1997) and Spaans & Carollo (1997) argue that more massive, spherical systems form stars earlier and for a shorter duration than less massive, more flattened systems. The models of Spaans & Carollo (1997) show that flattened systems lose metals more easily due to supernova blow-out, which has the consequence of delaying metal enrichment in the outer regions and thus delaying the peak of the star formation rate. This peak occurs when a metal-enriched multiphase ISM has built up, at which time gas can cool (and thus form stars) much more efficiently. By this argument, flattened galaxies — disky, power law profile, high $(v/\sigma)_*$, low mass — should have lower $[\alpha/\text{Fe}]$ and younger ages than boxy, core profile, low $(v/\sigma)_*$, high mass galaxies. Many of these predictions are confirmed, as mentioned above: a significant correlation is seen in the sense that smaller, less massive galaxies are younger than larger, more massive galaxies (Fig. 20); galaxies with power-law profiles have significantly lower $[\alpha/\text{Fe}]$ than galaxies with core profiles; and galaxies with disky isophotes have significantly lower $[\alpha/\text{Fe}]$ than galaxies with boxy isophotes. No statistically significant difference in age distribution is seen between core and power-law galaxies or boxy and disky galaxies, however, nor are any correlations between stellar population parameters and $(v/\sigma)_*$ found to be significant.

The models of Spaans & Carollo (1997) treat galaxies as evolving and forming stars in isolation. As Faber et al. (1997) summarized, gas-rich merger events lead naturally to disky galaxies with power-law profiles. Simulations (e. g. Barnes & Hernquist 1996) show that gas can destroy box orbits and that the gas (and thus star formation) in the remnant object is centrally concentrated. However, Faber et al. (1997) also noted that the merger of the supermassive black holes from the progenitor galaxies can produce core brightness profiles by ejecting stars from the center of the merger remnant. It is therefore unclear to what extent major mergers are expected to yield correlations between structural and stellar population parameters.

To search for additional correlations, principal component analyses were run on several combinations of parameters (Table 6). The input parameters were each reduced to zero mean and unit variance prior to the analysis. Combinations of parameters including luminosity (M_V), one structural variable (γ or the break radius r_b), and one SSP variable were studied; in addition, all seven galaxy parameters were analyzed together. Using the Kaiser criterion (Kaiser 1960), only those principal components which account for at least as much variance as

a single normalized input variable are listed in Table 6. No new planes were discovered in which two orthogonal linear combinations of the input variables could explain almost all of the variance in the three dimensional input parameter space. The distributions of galaxies in the parameter spaces studied by this method are triaxial, in some cases close to prolate spheroids and in other cases close to oblate spheroids.

4. SUMMARY AND CONCLUSIONS

A new set of spectra of nearby elliptical galaxies has been obtained. Combining this new data set with a selected portion of the G93 sample, a volume-limited sample of 45 galaxies has been defined, of which 35 have been observed. The ten missing galaxies have a distribution in luminosity and velocity dispersion that is similar to the full set of 45 galaxies.

It is worth noting that there is no significant qualitative difference between SSP models; for almost all galaxies the use of different models produces only a systematic offset in stellar population parameters. Although different choices of models will result in different absolute SSP quantities, comparing one galaxy to another within the same set of models yields consistent results independent of the choice of models. This quantitative offset between different models is greatest when higher order Balmer lines such as $H\gamma$ are used as the age-sensitive index in age-metallicity grids. The difference in ages derived using different sets of models is found to be greater than the difference in ages derived using different Balmer indices in model grids.

A method to constrain the input parameters for a two-burst multiple stellar population analysis has been proposed. However, stellar population data are available for the GC systems of only a few galaxies; four such galaxies are investigated here. In none of these cases is a two-burst model based on GC age measurements viable. Two galaxies are coeval with their GC populations, suggesting that SSP analysis is adequate for those galaxies. The other two galaxies have SSP ages significantly younger than any of the associated GCs.

The existence of the metallicity hyper-plane and the Z -plane of TFWG is confirmed by this new data set. The distribution of galaxies within these planes is very similar to that shown by TFWG, and this distribution is shown to be due to physical variations well in excess of measurement uncertainties.

The G93 galaxy sample analyzed by TFWG is representative of the local early-type galaxy population. This work is in good statistical agreement with their results.

Comparisons between stellar population parameters and indicators of a galaxy's internal structure support the idea introduced by Spaans & Carollo (1997) that size and angular momentum (i.e. large and spherical compared to smaller and flattened) are key distinctions between power law and core profile galaxies. Disky, power-law profile galaxies are found to have significantly lower $[\alpha/\text{Fe}]$ than boxy, core profile galaxies, though no significant trend in age is seen between core and power-law or boxy and disky galaxies. Age is found to decrease with size, measured either by radius or mass, as expected in downsizing models for galaxy formation.

This research has made use of the NASA/IPAC Extragalactic Database (NED) which is operated by the Jet Propulsion Laboratory, California Institute of Technology, under contract with the National Aeronautics and Space Administration. This work also made use of the Gauss-Hermite Pixel Fitting Software developed by R.P. van der Marel. J. H. H. was supported in part by an ARCS Fellowship. We would like to thank R. Schiavon, S. Faber, P. Guhathakurta, J. Brodie, R. Peterson, M. Bolte, J. Primack, M. Geha, J. Gonzalez, S. Trager, and S. Thorsett for helpful discussions, and S. Faber and T. Lauer for allowing the use of their results in advance of publication. We also thank the referee, Jim Rose, for his detailed comments which greatly improved the final paper.

REFERENCES

Baade, W. & Gaposchkin, C. H. P. 1963, Cambridge, Harvard University Press, 1963.,

Barnes, J. E. & Hernquist, L. 1996, *ApJ*, 471, 115

Bassin, M., & Bonatto, C. 2003, *A&A*, 410, 803

Bender, R., Burstein, D., & Faber, S. M. 1992, *ApJ*, 399, 462

Bender, R., Burstein, D., & Faber, S. M. 1993, *ApJ*, 411, 153

Beuing, J., Bender, R., Mendes de Oliveira, C., Thomas, D., & Maraston, C. 2002, *A&A*, 395, 431

Brodie, J. P., Strader, J., Denicoló, G., Beasley, M. A., Cenarro, A. J., Larsen, S. S., Kuntschner, H., & Forbes, D. A. 2005, *AJ*, 129, 2643

Burkert, A. 1993, *A&A*, 278, 23

Carollo, C. M., Danziger, I. J., Rich, R. M., & Chen, X. 1997, *ApJ*, 491, 545

Caldwell, N., Rose, J. A., & Concannon, K. D. 2003, *AJ*, 125, 2891

Cowie, L. L., Songaila, A., Hu, E. M., & Cohen, J. G. 1996, *AJ*, 112, 839

Denicoló, G., Terlevich, R., Terlevich, E., Forbes, D. A., Terlevich, A., & Carrasco, L. 2005, *MNRAS*, 356, 1440

de Vaucouleurs, G. 1948, *Ann. Astrophys.*, 11, 247

Faber, S. M., Wegner, G., Burstein, D., Davies, R. L., Dressler, A., Lynden-Bell, D., & Terlevich, R. J. 1989, *ApJS*, 69, 763

Faber, S. M., et al. 1997, *AJ*, 114, 1771

Gebhardt, K., et al. 2003, *ApJ*, 597, 239

Gonzalez, J. J. 1993, Ph.D. thesis, University of California, Santa Cruz (G93)

Howell, J. H. 2005, submitted

Howell, J. H., Brodie, J. P., Strader, J., Forbes, D. A., & Proctor, R. 2004, *AJ*, 128, 2749

Idiart, T. P., Michard, R. & de Freitas Pacheco, J. A. 2002, *A&A*, 383, 30

Jones, L.A. 1999, PhD Thesis, University of North Carolina

Jørgensen, I. 1997, *MNRAS*, 288, 161

Jørgensen, I. 1999, *MNRAS*, 306, 607

Kaiser, H. F. 1960, *Education and Psychological Measurement*, 20, 141

Kuntschner, H. & Davies, R. L. 1998, *MNRAS*, 295, L29

Kuntschner, H., Smith, R. J., Colless, M., Davies, R. L., Kaldare, R. & Vazdekis, A. 2002, *MNRAS*, 337, 172

Kuntschner, H., Ziegler, B. L., Sharples, R. M., Worthey, G., & Fricke, K. J. 2002, *A&A*, 395, 761

Larsen, S. S., Brodie, J. P., Beasley, M. A., Forbes, D. A., Kissler-Patig, M., Kuntschner, H., & Puzia, T. H. 2003, *ApJ*, 585, 767

Larson, R. B. 1974, *MNRAS*, 166, 585

Lauer, T. R., et al. 2005, *AJ*, 129, 2138

Longhetti, M., Bressan, A., Chiosi, C., & Rampazzo, R. 2000, *A&A*, 353, 917

Puzia, T. H., Zepf, S. E., Kissler-Patig, M., Hilker, M., Minniti, D., & Goudrooij, P. 2002, *A&A*, 391, 453

Puzia, T. H. 2003, Ph.D. Thesis, Ludwig-Maximilians-Universitaet Muenchen

Puzia, T. H., Kissler-Patig, M., Thomas, D., Maraston, C., Saglia, R. P., Bender, R., Richtler, T., Goudrooij, P., & Hempel, M. 2004, *A&A*, 415, 123

Rich, R. M. 1998, *ASP Conf. Ser.* 147, *Abundance Profiles: Diagnostic Tools for Galaxy History*, ed. D. Friedli, M. Edmunds, C. Robert, & L. Drissen (San Francisco: ASP), p. 36

Rose, J. A., Bower, R. G., Caldwell, N., Ellis, R. S., Sharples, R. M., & Teague, P. 1994, *AJ*, 108, 2054

Schechter, P. 1976, *ApJ*, 203, 297

Schiavon, R. 2005, in preparation

Spaans, M. & Carollo, C. M. 1997, *ApJ*, 482, L93

Strader, J. & Brodie, J. 2004, *AJ*, 128, 1671

Tantalo, R., Chiosi, C., & Bressan, A. 1998, *A&A*, 333, 419

Terlevich, A. I., & Forbes, D. A. 2002, *MNRAS*, 330, 547

Thomas, D., Maraston, C., & Bender, R. 2003, *MNRAS*, 339, 897

Thomas, D., Maraston, C., & Korn, A. 2004, *MNRAS*, 351, L19

Tonry, J. L., Dressler, A., Blakeslee, J. P., Ajhar, E. A., Fletcher, A. B., Luppino, G. A., Metzger, M. R., & Moore, C. B. 2001, *ApJ*, 546, 681

Trager, S. C., Worthey, G., Faber, S. M., & Gonzalez, J. J. 1998, *ApJS*, 116, 1

Trager, S. C., Faber, S. M., Worthey, G., & Gonzalez, J. J. 2000a, *AJ*, 119, 1645

Trager, S. C., Faber, S. M., Worthey, G., & Gonzalez, J. J. 2000b, *AJ*, 120, 165 (TFWG)

Trippico, M. J. & Bell, R. A. 1995, *AJ*, 110, 3035

van der Marel 1994, *MNRAS*, 270, 271

Worthey, G., Faber, S. M., Gonzalez, J. J., & Burstein, D. 1994, *ApJS*, 94, 687

Worthey, G. 1994, *ApJS*, 95, 107

Worthey, G., & Ottaviani, D. L. 1997, *ApJS*, 111, 377

Zepf, S. E. & Ashman, K. M. 1993, *MNRAS*, 264, 611

TABLE 1
VOLUME LIMITED GALAXY SAMPLE

Name	α (J2000)	δ (J2000)	S/N	Observed
NGC 584	01 ^h 31 ^m 20.7 ^s	-06 ^o 52'06"		G93
NGC 596	01 ^h 32 ^m 52.08 ^s	-07 ^o 01'54.6"	147.0	2002 November 3
NGC 720	01 ^h 53 ^m 00.4 ^s	-13 ^o 44'18"		G93
NGC 821	02 ^h 08 ^m 21.0 ^s	+10 ^o 59'44"		G93
NGC 1052	02 ^h 41 ^m 04.80 ^s	-08 ^o 15'20.8"	205.8	2000 November 26
NGC 1172	03 ^h 01 ^m 36.0 ^s	-14 ^o 50'11"	97.0	2002 November 3
NGC 1199	03 ^h 03 ^m 38.6 ^s	-15 ^o 36'51"		Not Observed
NGC 1209	03 ^h 06 ^m 03.0 ^s	-15 ^o 36'40"	149.2	2000 November 27
NGC 1400	03 ^h 39 ^m 31.0 ^s	-18 ^o 41'22"	121.0	2003 January 2
NGC 1407	03 ^h 40 ^m 11.8 ^s	-18 ^o 34'48"	164.3	2000 November 26
NGC 2768	09 ^h 11 ^m 37.50 ^s	+60 ^o 02'15.0"	89.7	2002 November 4
NGC 2974	09 ^h 42 ^m 32.96 ^s	-03 ^o 41'55.2"		Not Observed
NGC 3115	10 ^h 05 ^m 13.42 ^s	-07 ^o 43'06.5"	305.0	2001 March 28
NGC 3156	10 ^h 12 ^m 41.08 ^s	+03 ^o 07'50.2"		Not Observed
NGC 3193	10 ^h 18 ^m 24.88 ^s	+21 ^o 53'38.6"	108.9	2004 March 27
NGC 3226	10 ^h 23 ^m 27.00 ^s	+19 ^o 53'54.4"	101.9	2001 March 25
NGC 3607	11 ^h 16 ^m 54.08 ^s	+18 ^o 03'11.6"	141.0	2003 January 2
NGC 3608	11 ^h 16 ^m 58.7 ^s	+18 ^o 08'57"		G93
NGC 3610	11 ^h 18 ^m 25.83 ^s	+58 ^o 47'13.6"	136.4	2001 March 27
NGC 3613	11 ^h 18 ^m 36.12 ^s	+58 ^o 00'04.5"	107.4	2001 March 27
NGC 3640	11 ^h 21 ^m 06.74 ^s	+03 ^o 14'08.1"	151.9	2001 March 28
NGC 3962	11 ^h 54 ^m 40.0 ^s	-13 ^o 58'30"		Not Observed
NGC 4125	12 ^h 08 ^m 05.71 ^s	+65 ^o 10'24.5"		Not Observed
NGC 4168	12 ^h 12 ^m 16.9 ^s	+13 ^o 12'20"	103.7	2001 March 25
NGC 4278	12 ^h 20 ^m 06.82 ^s	+29 ^o 16'50.7"		Not Observed
NGC 4365	12 ^h 24 ^m 27.87 ^s	+07 ^o 19'04.9"	158.3	2001 March 26
NGC 4374	12 ^h 25 ^m 03.7 ^s	+12 ^o 53'14"		G93
NGC 4406	12 ^h 26 ^m 11.74 ^s	+12 ^o 56'46.4"		Not Observed
NGC 4472	12 ^h 29 ^m 46.5 ^s	+07 ^o 59'48"		G93
NGC 4473	12 ^h 29 ^m 48.87 ^s	+13 ^o 25'45.7"	186.7	2001 March 28
NGC 4486	12 ^h 30 ^m 49.42 ^s	+12 ^o 23'28.0"	150.9	2004 March 27
NGC 4552	12 ^h 35 ^m 39.9 ^s	+12 ^o 33'55"		G93
NGC 4621	12 ^h 42 ^m 02.49 ^s	+11 ^o 38'48.7"	166.3	2004 March 27
NGC 4636	12 ^h 42 ^m 49.7 ^s	+02 ^o 41'18.4"		Not Observed
NGC 4649	12 ^h 43 ^m 39.7 ^s	+11 ^o 33'09"		G93
NGC 4697	12 ^h 48 ^m 35.8 ^s	-05 ^o 48'00"		G93
NGC 5322	13 ^h 49 ^m 15.19 ^s	+60 ^o 11'26.2"		Not Observed
NGC 5485	14 ^h 07 ^m 11.5 ^s	+55 ^o 00'07"		Not Observed
NGC 5576	14 ^h 21 ^m 04.11 ^s	+03 ^o 16'13.5"	144.0	2001 March 26
NGC 5638	14 ^h 29 ^m 40.4 ^s	+03 ^o 14'04"		G93
NGC 5812	15 ^h 00 ^m 57.0 ^s	-07 ^o 27'19"		G93
NGC 5813	15 ^h 01 ^m 11.2 ^s	+01 ^o 42'08"		G93
NGC 5831	15 ^h 04 ^m 07.2 ^s	+01 ^o 13'15"		G93
NGC 5846	15 ^h 06 ^m 29.3 ^s	+01 ^o 36'21"	153.2	G93, 2001 March 28
NGC 6703	18 ^h 47 ^m 18.9 ^s	+45 ^o 33'02"		G93

TABLE 2
INDEX MEASUREMENTS: $r_e/8$ APERTURE

Galaxy	σ	Ca4227	G4300	$H\gamma_F$	Fe4383	Ca4455	Fe4531	C ₂ 4668	$H\beta$	[OIII]	Fe5015	Mg ₂	Mgb	Fe5270	Fe5335	Fe5406	[MgFe]'
NGC 596	151	1.19	5.33	-1.12	4.54	2.06	3.62	6.60	1.94	-0.06	5.43	0.260	3.89	2.91	2.46	1.72	3.29
	4	0.10	0.14	0.13	0.21	0.14	0.09	0.20	0.06	0.03	0.28	0.003	0.05	0.06	0.09	0.09	0.05
NGC 1052	215	1.20	5.72	-2.17	6.50	1.43	3.78	8.24	1.21	-3.71	1.90	0.340	5.96	3.05	2.78	1.88	4.21
	4	0.10	0.14	0.38	0.09	0.05	0.11	0.12	0.7	1.0	0.64	0.003	0.05	0.06	0.09	0.09	0.05
NGC 1172	113	1.21	5.29	-1.16	4.38	1.35	3.36	4.97	1.94	-0.65	4.91	0.238	3.89	2.70	2.27	1.61	3.17
	4	0.10	0.14	0.15	0.21	0.14	0.09	0.20	0.15	0.20	0.30	0.003	0.06	0.09	0.13	0.09	0.07
NGC 1209	225	1.39	5.35	-1.85	5.58	1.58	3.76	7.75	1.27	-0.23	5.91	0.326	4.99	3.32	2.78	1.72	3.98
	4	0.10	0.14	0.12	0.09	0.05	0.11	0.12	0.12	0.15	0.22	0.003	0.05	0.06	0.09	0.09	0.05
NGC 1400	285	1.39	5.08	-1.80	4.72	1.47	3.90	7.47	1.33	-0.21	6.03	0.336	5.32	3.01	2.75	1.82	3.95
	5	0.10	0.14	0.14	0.21	0.14	0.09	0.20	0.11	0.13	0.29	0.003	0.06	0.09	0.13	0.09	0.08
NGC 1407	296	1.47	4.80	-1.18	6.29	1.30	3.87	8.80	1.40	-0.01	5.90	0.350	5.41	3.50	2.83	1.86	4.23
	4	0.10	0.14	0.11	0.09	0.05	0.11	0.12	0.06	0.02	0.20	0.003	0.05	0.06	0.09	0.09	0.05
NGC 2768	211	1.46	5.36	-1.45	5.36	1.50	3.80	5.23	1.62	-0.58	4.29	0.200	4.36	2.81	2.70	1.92	3.48
	4	0.09	0.18	0.20	0.20	0.05	0.11	0.11	0.35	0.47	0.58	0.003	0.07	0.10	0.14	0.09	0.08
NGC 3115	276	1.55	5.57	-1.78	5.61	1.53	4.03	8.52	1.66	-0.03	6.23	0.325	5.04	3.33	3.21	2.07	4.08
	4	0.10	0.14	0.11	0.09	0.05	0.11	0.12	0.04	0.01	0.20	0.003	0.05	0.05	0.07	0.09	0.04
NGC 3193	228	1.27	5.17	-1.64	5.10	1.59	3.94	7.52	1.50	-0.45	5.28	0.318	4.61	3.02	2.67	2.16	3.67
	4	0.09	0.18	0.13	0.20	0.05	0.11	0.11	0.16	0.18	0.58	0.003	0.07	0.10	0.14	0.09	0.08
NGC 3226	180	1.09	5.85	-2.17	4.75	1.39	3.67	7.26	1.73	-1.48	4.14	0.294	4.73	2.78	2.77	1.78	3.62
	5	0.10	0.16	0.12	0.18	0.07	0.07	0.19	0.17	0.23	0.18	0.003	0.06	0.09	0.13	0.09	0.08
NGC 3607	231	1.14	5.27	-1.53	4.86	1.47	3.78	8.22	1.53	-0.30	5.89	0.313	4.76	2.96	2.78	1.83	3.72
	4	0.10	0.14	0.14	0.21	0.14	0.09	0.20	0.11	0.13	0.28	0.003	0.05	0.06	0.09	0.09	0.05
NGC 3610	172	0.89	4.99	-0.52	4.72	1.52	3.57	8.08	2.39	-0.03	5.51	0.255	4.04	2.77	3.10	1.81	3.40
	4	0.10	0.16	0.09	0.18	0.07	0.07	0.19	0.08	0.08	0.12	0.003	0.05	0.06	0.09	0.09	0.05
NGC 3613	221	1.29	5.16	-1.46	5.00	1.77	3.35	7.43	1.85	0.00	5.92	0.289	4.47	3.21	3.15	2.00	3.78
	4	0.10	0.16	0.08	0.18	0.07	0.07	0.19	0.06	0.01	0.11	0.003	0.06	0.09	0.13	0.09	0.07
NGC 3640	178	1.20	5.22	-1.29	4.88	1.51	3.61	6.83	1.87	-0.03	5.79	0.266	3.96	2.96	2.84	1.80	3.40
	4	0.10	0.16	0.08	0.18	0.07	0.07	0.19	0.06	0.02	0.11	0.003	0.05	0.06	0.09	0.09	0.05
NGC 4168	179	1.08	5.07	-1.08	4.85	1.59	3.52	6.65	1.87	-0.26	5.06	0.258	3.98	2.92	2.69	1.61	3.37
	5	0.10	0.16	0.08	0.18	0.07	0.07	0.19	0.07	0.05	0.11	0.003	0.06	0.09	0.13	0.09	0.07
NGC 4365	270	1.58	5.41	-1.48	5.24	1.95	4.04	8.78	1.55	-0.01	5.57	0.330	5.18	3.32	3.19	2.07	4.12
	4	0.10	0.16	0.08	0.18	0.07	0.07	0.19	0.06	0.01	0.11	0.003	0.05	0.06	0.09	0.09	0.05
NGC 4473	201	1.31	5.62	-2.01	5.48	1.70	3.79	7.64	1.74	-0.01	5.73	0.315	4.73	3.22	3.02	1.81	3.87
	4	0.10	0.16	0.08	0.18	0.07	0.07	0.19	0.06	0.01	0.11	0.003	0.05	0.06	0.09	0.09	0.05
NGC 4486	371	1.71	5.47	1.37	5.71	1.30	4.24	8.71	1.07	-0.57	3.63	0.348	5.78	2.88	3.22	2.37	4.15
	5	0.09	0.18	0.16	0.20	0.05	0.11	0.11	0.25	0.32	0.58	0.003	0.06	0.07	0.11	0.09	0.07
NGC 4621	260	1.45	5.50	-2.07	5.34	1.54	4.03	8.39	1.26	0.0	5.66	0.348	5.09	3.15	3.07	2.15	3.99
	4	0.09	0.18	0.11	0.20	0.05	0.11	0.11	0.10	0.01	0.58	0.003	0.06	0.07	0.11	0.09	0.07
NGC 5576	190	1.10	5.36	-1.04	4.66	1.41	3.57	7.32	2.10	-0.01	5.52	0.271	4.13	3.03	2.83	1.79	3.50
	4	0.10	0.16	0.08	0.18	0.07	0.07	0.19	0.06	0.02	0.11	0.003	0.05	0.06	0.09	0.09	0.05
NGC 5846	243	1.40	5.09	-1.16	5.39	1.51	3.70	8.12	1.44	-0.23	4.81	0.333	5.20	3.13	3.03	1.91	4.02
	4	0.10	0.16	0.10	0.18	0.07	0.07	0.19	0.12	0.15	0.11	0.003	0.05	0.06	0.09	0.09	0.05

TABLE 3
PRIMARY INDEX ERROR TABLE

Error	$H\beta$	Mgb	Fe5270	Fe5335
Simulations	0.05	0.03	0.04	0.06
Velocity Dispersion	0.00	0.00	0.01	0.02
Calibration - External	0.05	0.05	0.04	0.06
Calibration - Internal	0.02	0.02	0.02	0.04
Lick/IDS System	0.07	0.07	0.08	0.08

TABLE 4
STELLAR POPULATION PARAMETERS

Galaxy	σ (km/s)	σ_σ (km/s)	Age (Gyr)	σ_t (Gyr)	[Z/H] (dex)	σ_Z (dex)	$[\alpha/\text{Fe}]$ (dex)	σ_α (dex)
This work, TMB models:								
NGC 0596	151	4	4.4	0.7	0.22	0.1	0.19	0.04
NGC 1052	215	4	16	14	0.42	0.3	0.44	0.12
NGC 1172	113	4	4.8	1.5	0.13	0.13	0.26	0.05
NGC 1209	225	4	15.6	3.0	0.28	0.08	0.23	0.03
NGC 1400	285	5	14.2	3.0	0.31	0.13	0.35	0.04
NGC 1407	296	4	9.5	2.2	0.56	0.07	0.30	0.04
NGC 2768	211	4	10	7.0	0.14	0.25	0.22	0.10
NGC 3115	276	4	3.9	0.7	0.65	0.06	0.25	0.03
NGC 3193	228	4	11.8	3.2	0.20	0.12	0.24	0.06
NGC 3226	180	5	6.1	3.5	0.33	0.17	0.32	0.06
NGC 3607	231	4	10.6	2.3	0.27	0.1	0.27	0.04
NGC 3610	172	4	1.7	0.1	0.76	0.16	0.28	0.03
NGC 3613	221	4	3.3	1.0	0.59	0.12	0.17	0.05
NGC 3640	178	4	4.9	1.0	0.26	0.08	0.13	0.04
NGC 4168	179	5	5.0	1.4	0.24	0.1	0.17	0.05
NGC 4365	270	4	5.9	1.9	0.59	0.08	0.26	0.04
NGC 4473	201	4	4.0	1.3	0.56	0.08	0.24	0.04
NGC 4486	371	5	19.6	7.5	0.27	0.18	0.36	0.08
NGC 4621	260	4	15.8	4.0	0.29	0.11	0.23	0.05
NGC 5576	190	4	2.5	0.4	0.60	0.11	0.21	0.05
NGC 5846	243	4	10.6	4.4	0.44	0.14	0.28	0.03
Galaxies from G93, volume-limited sample, TMB models:								
NGC 0584	236	3	2.4	0.3	0.61	0.04	0.24	0.03
NGC 0720	239	5	3.7	1.8	0.55	0.09	0.40	0.08
NGC 0821	189	3	7.3	1.5	0.33	0.02	0.22	0.03
NGC 3608	178	3	6.1	1.5	0.38	0.04	0.24	0.04
NGC 4374	282	3	11.1	1.5	0.24	0.02	0.28	0.02
NGC 4472	279	4	7.8	1.5	0.36	0.04	0.29	0.03
NGC 4552	252	3	10.5	1.5	0.36	0.03	0.31	0.02
NGC 4649	310	3	11.9	1.5	0.37	0.03	0.32	0.02
NGC 4697	162	4	7.1	1.8	0.19	0.04	0.18	0.03
NGC 5638	154	3	7.8	1.5	0.32	0.03	0.26	0.03
NGC 5812	200	3	5.0	1.1	0.47	0.03	0.26	0.03
NGC 5813	205	3	14.9	2.3	0.07	0.04	0.29	0.03
NGC 5831	161	3	2.7	0.2	0.61	0.04	0.20	0.03
NGC 5846	224	4	12.2	2.4	0.25	0.04	0.29	0.03
NGC 6703	183	3	3.9	1.0	0.39	0.05	0.21	0.03
Other galaxies from G93, TMB models:								
NGC 0221	72	3	2.8	0.7	0.10	0.05	-0.07	0.01
NGC 0315	321	4	5.0	1.5	0.44	0.06	0.32	0.02
NGC 0507	262	6	6.9	2.8	0.29	0.07	0.27	0.03
NGC 0547	236	4	8.3	2.4	0.34	0.05	0.33	0.02
NGC 0636	160	3	3.8	0.7	0.44	0.07	0.18	0.02
NGC 1453	286	4	7.1	1.9	0.42	0.06	0.29	0.02
NGC 1600	315	4	7.6	2.2	0.47	0.06	0.30	0.02
NGC 1700	227	3	2.3	0.7	0.63	0.10	0.17	0.03
NGC 2300	252	3	5.5	1.5	0.48	0.05	0.32	0.02
NGC 2778	154	3	5.0	1.8	0.40	0.09	0.30	0.03
NGC 3377	108	3	3.5	0.8	0.30	0.06	0.27	0.02
NGC 3379	203	3	8.0	1.4	0.32	0.03	0.28	0.01
NGC 3818	173	4	5.2	1.8	0.47	0.08	0.30	0.03
NGC 4261	288	3	14.5	3.3	0.29	0.04	0.27	0.01
NGC 4478	128	2	4.3	2.3	0.40	0.10	0.22	0.03
NGC 4489	47	4	2.3	0.4	0.24	0.06	0.04	0.02
NGC 6127	239	4	10.8	2.2	0.28	0.04	0.30	0.02
NGC 6702	174	3	1.4	0.1	0.80	0.07	0.16	0.03
NGC 7052	274	4	11.7	3.1	0.27	0.05	0.31	0.02
NGC 7454	106	3	4.7	1.0	0.04	0.04	0.13	0.02
NGC 7562	248	3	7.1	1.6	0.31	0.04	0.24	0.01
NGC 7619	300	3	13.5	2.2	0.31	0.03	0.25	0.01
NGC 7626	253	3	12.0	2.4	0.27	0.03	0.32	0.01
NGC 7785	240	3	7.9	2.3	0.31	0.05	0.23	0.02

TABLE 5
SUPPLEMENTARY PARAMETERS

Galaxy	M_B	$\log r_e$ (pc)	$(v/\sigma)_*$	γ	Δ_{BV}
Galaxies from this work:					
NGC 0596	-19.58	3.41	0.67	0.16	—
NGC 1052	-20.11	3.53	1.00	0.18	—
NGC 1172	-19.48	3.68	—	-0.01	—
NGC 1209	-19.72	3.40	—	—	—
NGC 1400	-20.16	3.62	—	-0.10	—
NGC 1407	-21.21	3.90	0.84	—	—
NGC 2768	-20.26	3.65	—	0.24	-0.054
NGC 3115	-20.30	3.29	1.25	0.52	-0.069
NGC 3193	-20.28	3.48	0.80	0.01	-0.086
NGC 3226	-20.16	3.83	—	0.00	—
NGC 3607	-21.24	3.86	0.92	0.26	-0.067
NGC 3610	-20.28	3.19	1.10	0.76	-0.075
NGC 3613	-19.99	3.44	0.84	0.04	-0.074
NGC 3640	-19.99	3.63	1.48	-0.10	-0.043
NGC 4168	-20.18	3.77	0.22	0.17	—
NGC 4365	-20.34	3.64	0.08	0.07	-0.058
NGC 4473	-19.77	3.28	0.40	-0.07	-0.063
NGC 4486	-21.46	3.90	0.11	0.27	-0.063
NGC 4621	-20.33	3.55	0.74	0.75	-0.081
NGC 5576	-19.84	3.29	0.22	0.01	-0.076
NGC 5846	-21.15	4.02	0.10	—	-0.051
Galaxies from G93, volume-limited sample:					
NGC 0584	-20.39	3.48	1.55	-0.01	—
NGC 0720	-21.16	3.75	0.32	0.06	—
NGC 0821	-20.27	3.64	0.70	0.10	—
NGC 3608	-20.19	3.61	0.27	0.09	-0.064
NGC 4374	-21.39	3.68	0.09	0.15	-0.044
NGC 4472	-21.81	3.93	0.43	0.01	-0.040
NGC 4552	-20.44	3.36	0.28	-0.10	-0.080
NGC 4649	-21.51	3.80	0.42	0.16	-0.053
NGC 4697	-20.36	3.65	0.71	0.22	—
NGC 5638	-20.12	3.65	0.73	—	—
NGC 5812	-20.40	3.47	0.52	0.59	—
NGC 5813	-21.20	3.90	0.51	-0.10	-0.045
NGC 5831	-19.94	3.57	0.19	0.33	-0.078
NGC 6703	-20.21	3.50	0.30	—	—
Other galaxies from G93:					
NGC 0221	-15.91	2.20	0.89	0.00	—
NGC 0315	-22.15	4.23	0.09	—	—
NGC 0507	-21.74	4.35	0.09	0.00	—
NGC 0547	-21.20	3.91	0.24	—	—
NGC 0636	-20.23	3.45	1.04	—	—
NGC 1453	-21.33	3.85	0.62	—	—
NGC 1600	-22.23	4.17	0.03	-0.03	—
NGC 2300	-20.38	3.65	0.08	0.07	—
NGC 2778	-18.67	3.34	0.74	0.33	—
NGC 3377	-19.26	3.28	0.86	0.03	-0.075
NGC 3379	-20.02	3.27	0.72	0.18	-0.043
NGC 3818	-20.41	3.58	0.93	—	—
NGC 4261	-21.22	3.79	0.10	0.16	-0.089
NGC 4478	-19.16	3.11	0.84	-0.10	-0.103
NGC 4489	-18.46	3.46	1.49	—	—
NGC 6127	-21.03	3.82	0.11	—	—
NGC 6702	-20.55	3.87	0.18	—	—
NGC 7052	-21.14	3.96	0.34	0.16	—
NGC 7454	-19.34	3.49	0.13	—	—
NGC 7562	-21.50	3.86	0.06	—	—
NGC 7619	-21.77	3.93	0.53	-0.02	—
NGC 7626	-21.03	3.88	0.12	0.47	—
NGC 7785	-20.91	3.78	0.47	-0.10	—

TABLE 6
PRINCIPAL COMPONENT ANALYSIS TABLE

Input Parameters	% of variance	Principal Component
$M_V, \gamma, \log(t)$	52	$PC1 = -0.305M_V - 0.681\gamma + 0.666\log(t)$
$M_V, \gamma, [Z/H]$	54	$PC1 = 0.170M_V + 0.731\gamma + 0.661[Z/H]$
$M_V, \gamma, [\alpha/Fe]$	45	$PC1 = -0.258M_V - 0.702\gamma + 0.663[\alpha/Fe]$
	38	$PC2 = 0.665\gamma + 0.741[\alpha/Fe]$
$M_V, \log(r_b), \log(t)$	64	$PC1 = 0.634M_V - 0.618\log(r_b) - 0.466\log(t)$
$M_V, \log(r_b), [Z/H]$	49	$PC1 = 0.433M_V - 0.898\log(r_b)$
	39	$PC2 = 0.111M_V + 0.993[Z/H]$
$M_V, \log(r_b), [\alpha/Fe]$	56	$PC1 = 0.328M_V - 0.735\log(r_b) - 0.594[\alpha/Fe]$
$M_V, \gamma, \log(r_b), \log(\sigma), \log(t), [Z/H], [\alpha/Fe]$	38	$PC1 = -0.275M_V - 0.346\gamma + 0.460\log(r_b) + 0.467\log(\sigma) + 0.446\log(t) - 0.200[Z/H] + 0.369[\alpha/Fe]$
	25	$PC2 = 0.287\gamma + 0.160\log(r_b) + 0.373\log(\sigma) - 0.360\log(t) + 0.702[Z/H] + 0.351[\alpha/Fe]$
	20	$PC3 = -0.591\gamma + 0.527\log(r_b) - 0.304\log(\sigma) - 0.436\log(t) + 0.175[Z/H] - 0.242[\alpha/Fe]$

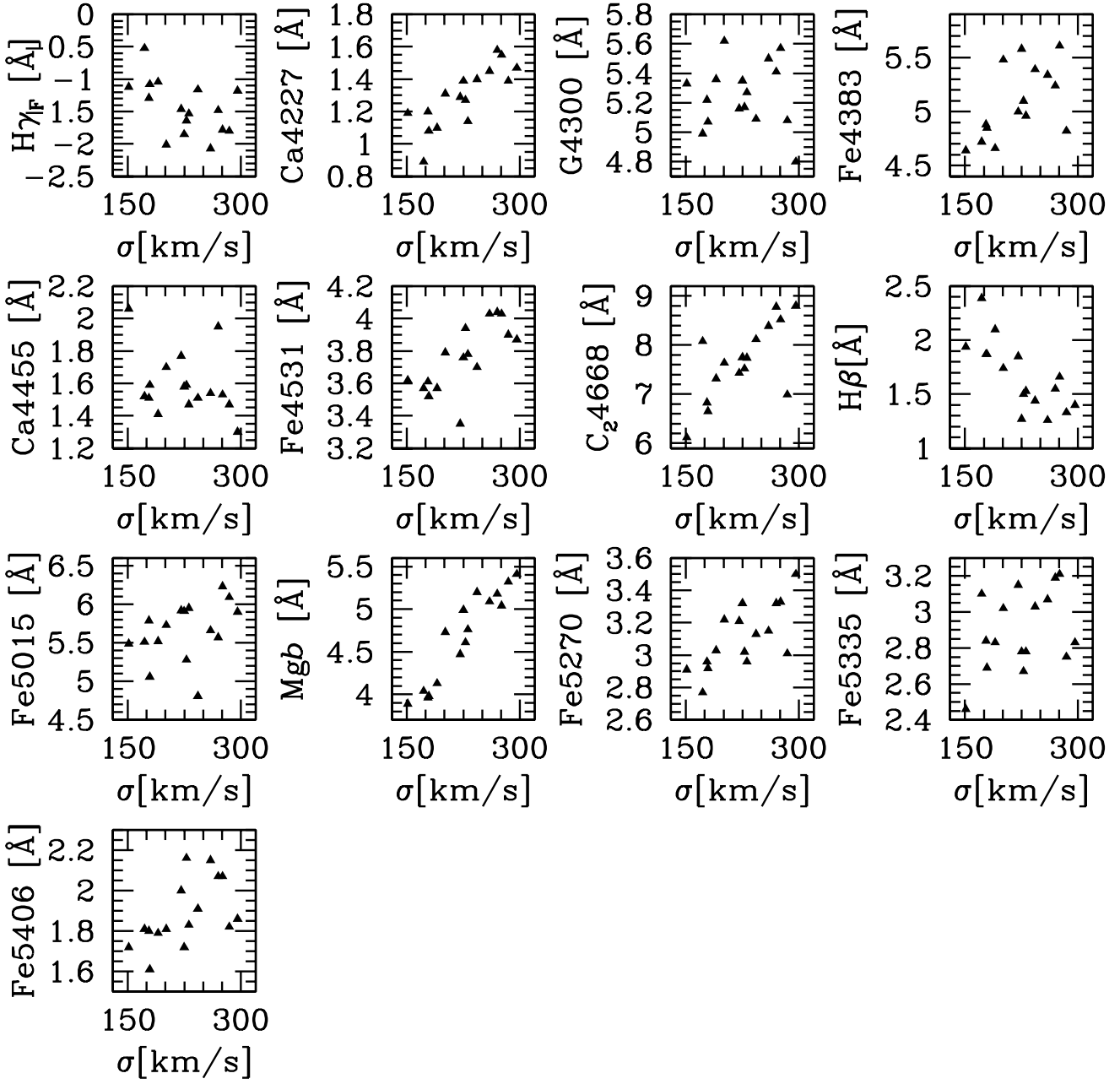


FIG. 1.— Spectral indices plotted against galaxy velocity dispersion. The Mg– σ relation is clearly apparent, as are similar but noisier relations in Ca4227, C₂4668, and the iron indices. A relation in the opposite direction (smaller index value at larger σ) is seen in H β and H γ .

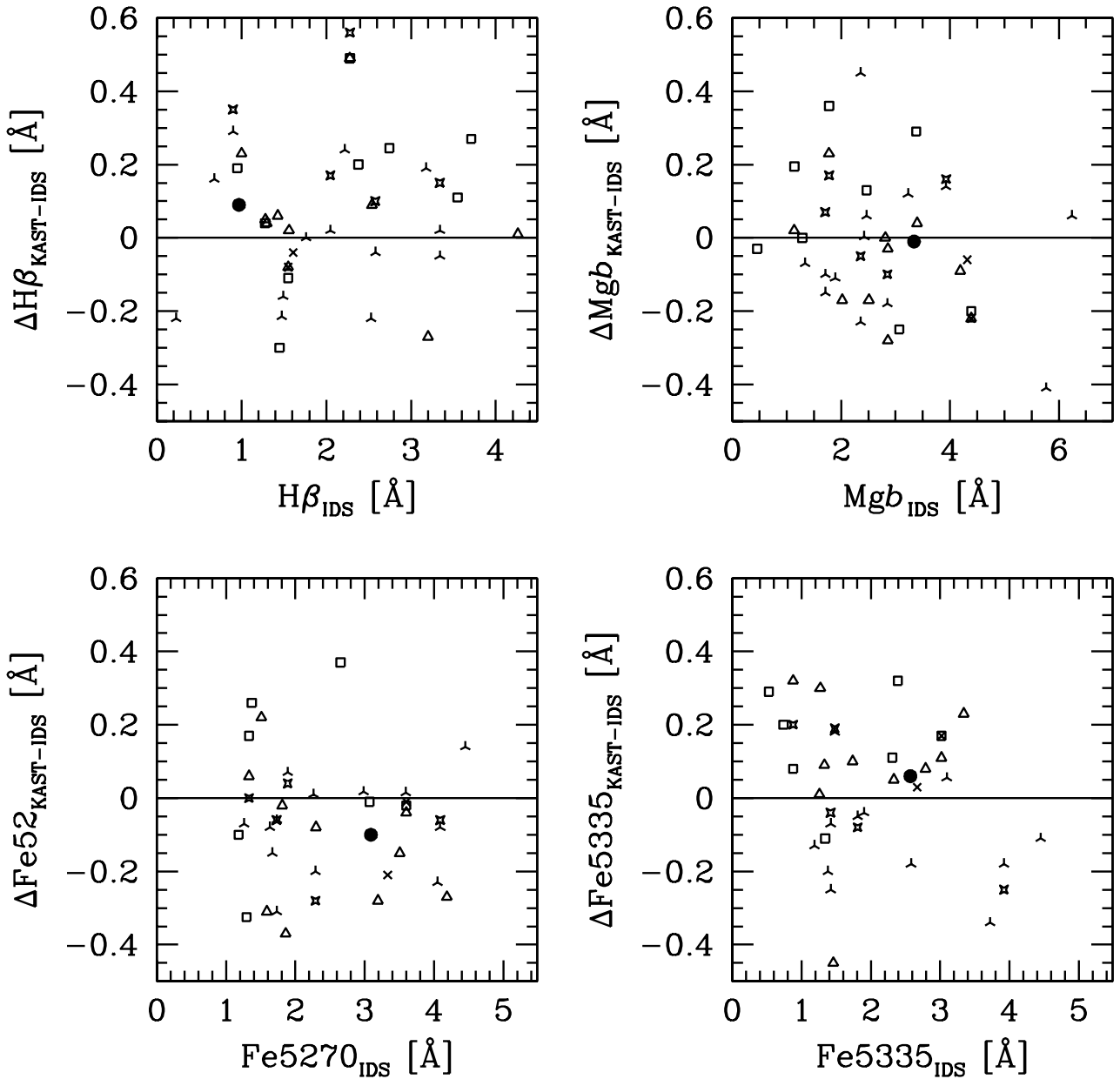


FIG. 2.— Comparisons of standard star primary index measurements to the Lick/IDS sample of Worthey et al. (1994). Different point types represent different observing runs. The large solid circle represents HD 51440, an internal standard star for the Lick/IDS system and as such the most accurately measured data point in this figure. No calibration correction has been applied to these data points. The calibration uncertainty shown here is a major limitation on the overall index uncertainty, as the calibration error often dominates the error budget.

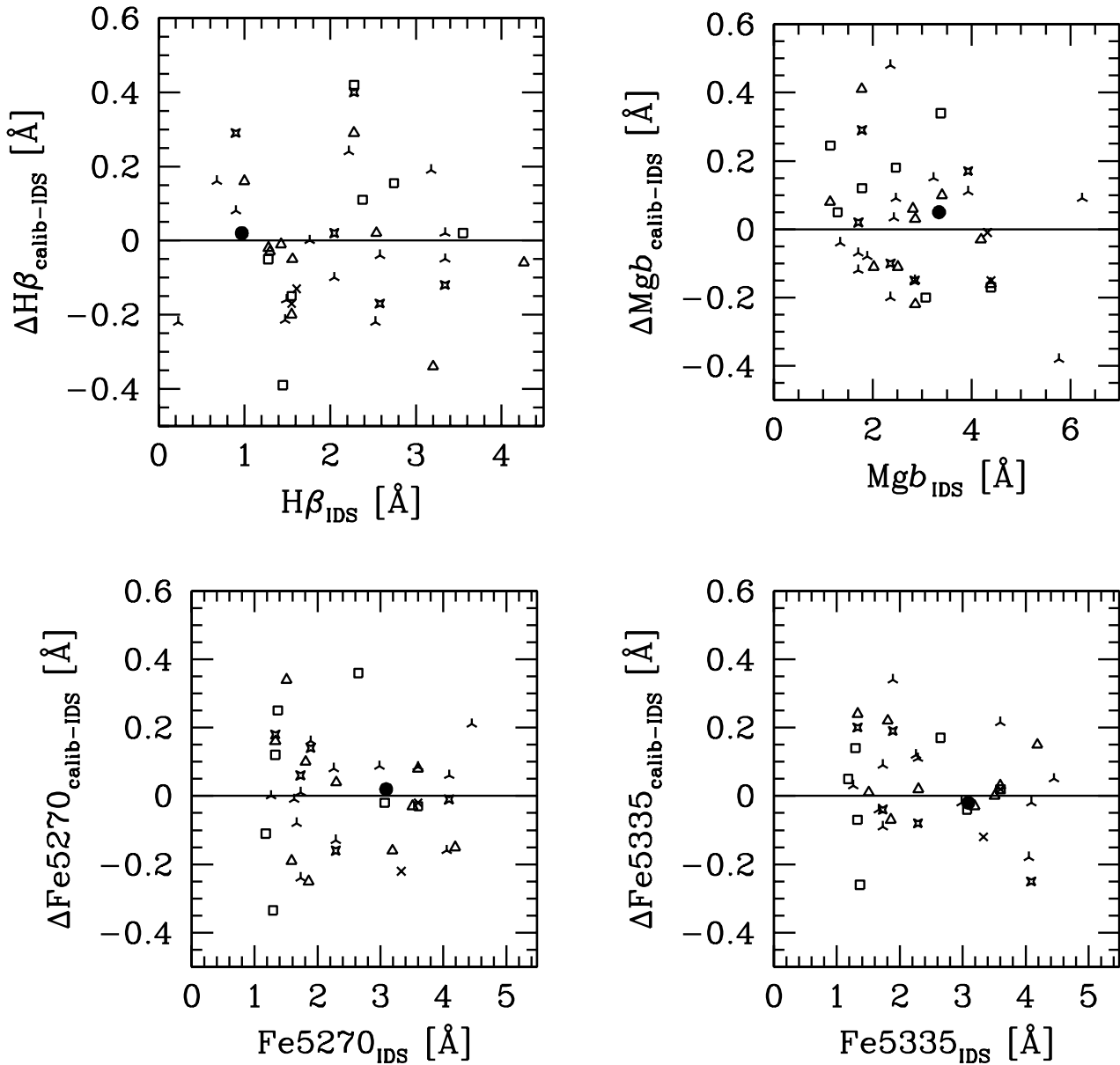


FIG. 3.— Comparisons of standard star primary index measurements to the Lick/IDS sample of Worthey et al. (1994). Different point types represent different observing runs as above. A constant calibration offset has been applied to each observing run; the 2002 November and 2003 January runs have been combined for this purpose due to the limited number of standard stars observed in each. No trend with index strength is seen, confirming that a constant offset is sufficient to calibrate the data onto the Lick/IDS system.

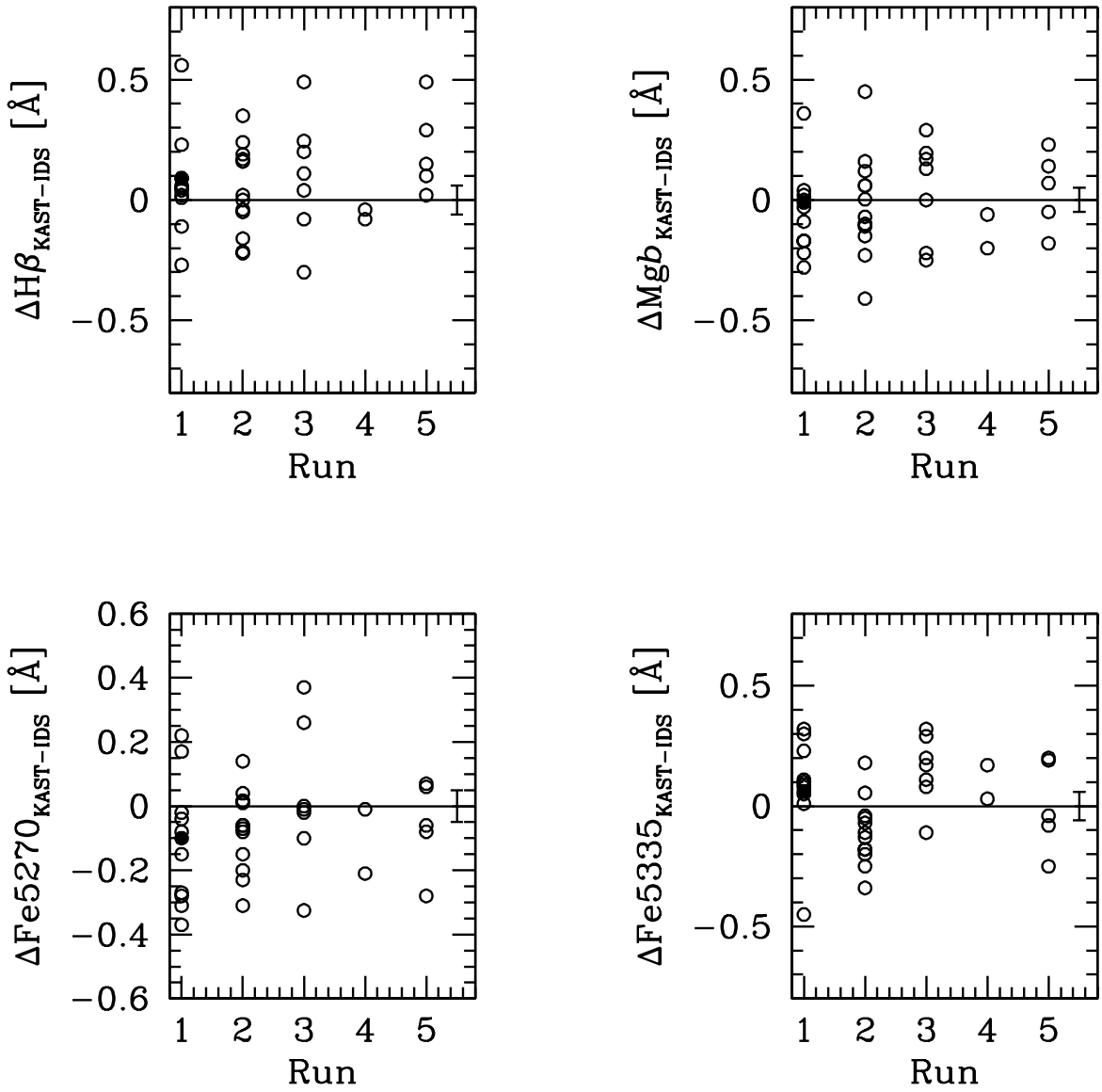


FIG. 4.— Comparisons of uncorrected standard star primary index measurements to the Lick/IDS sample of Worthey et al. (1994). The solid point is HD 51440, one of the internal standard stars for the IDS system; as such it is more accurately measured than any other star in this data set. Also shown is the typical error in the mean for the index offsets within a given observing run. The run to run variations in the mean index values are apparent.

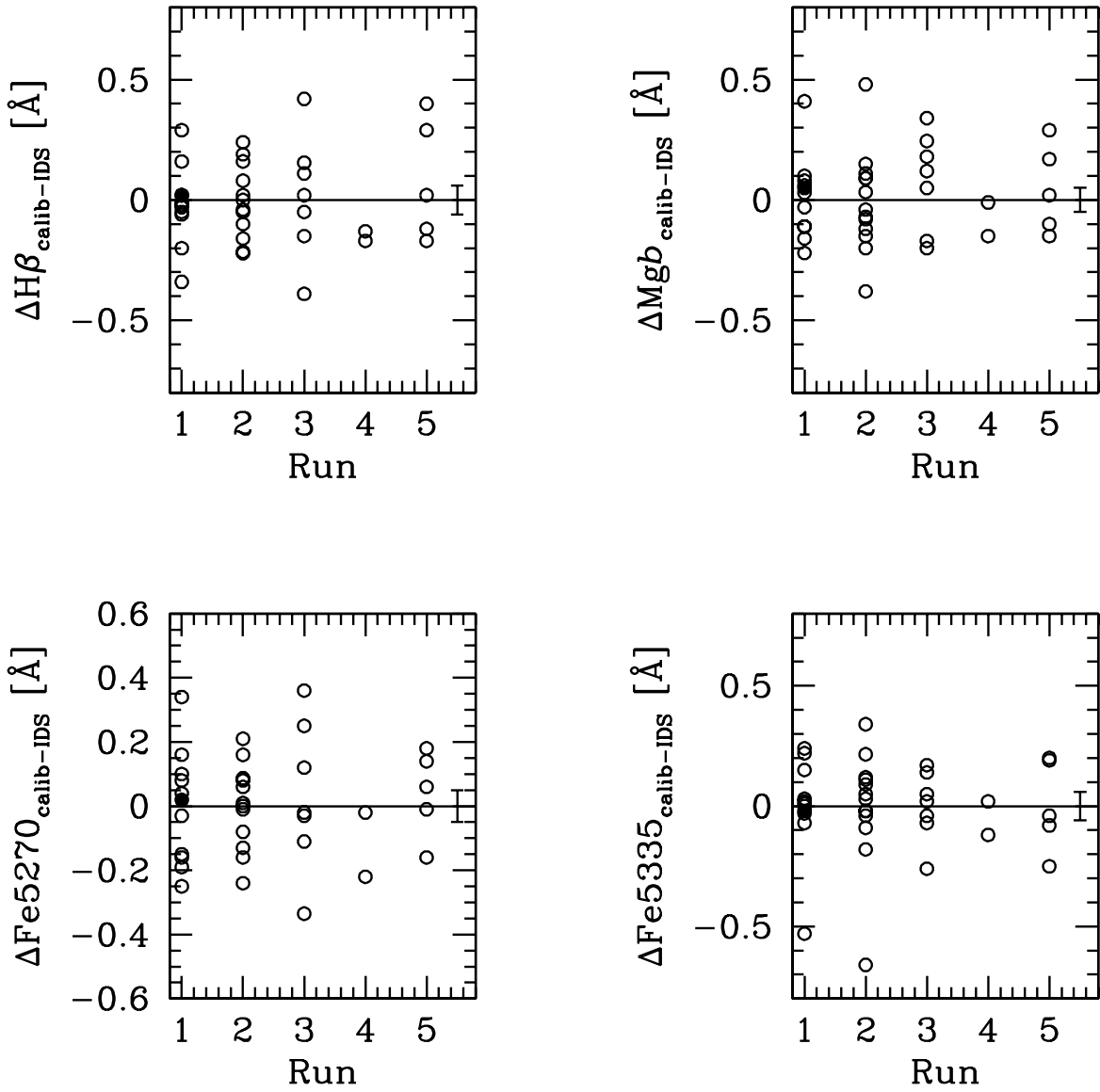


FIG. 5.— As in Fig. 4, after correcting the observations to the Lick/IDS system. The offset for each run was determined separately except for Runs 4 and 5 which were combined for calibration purposes.

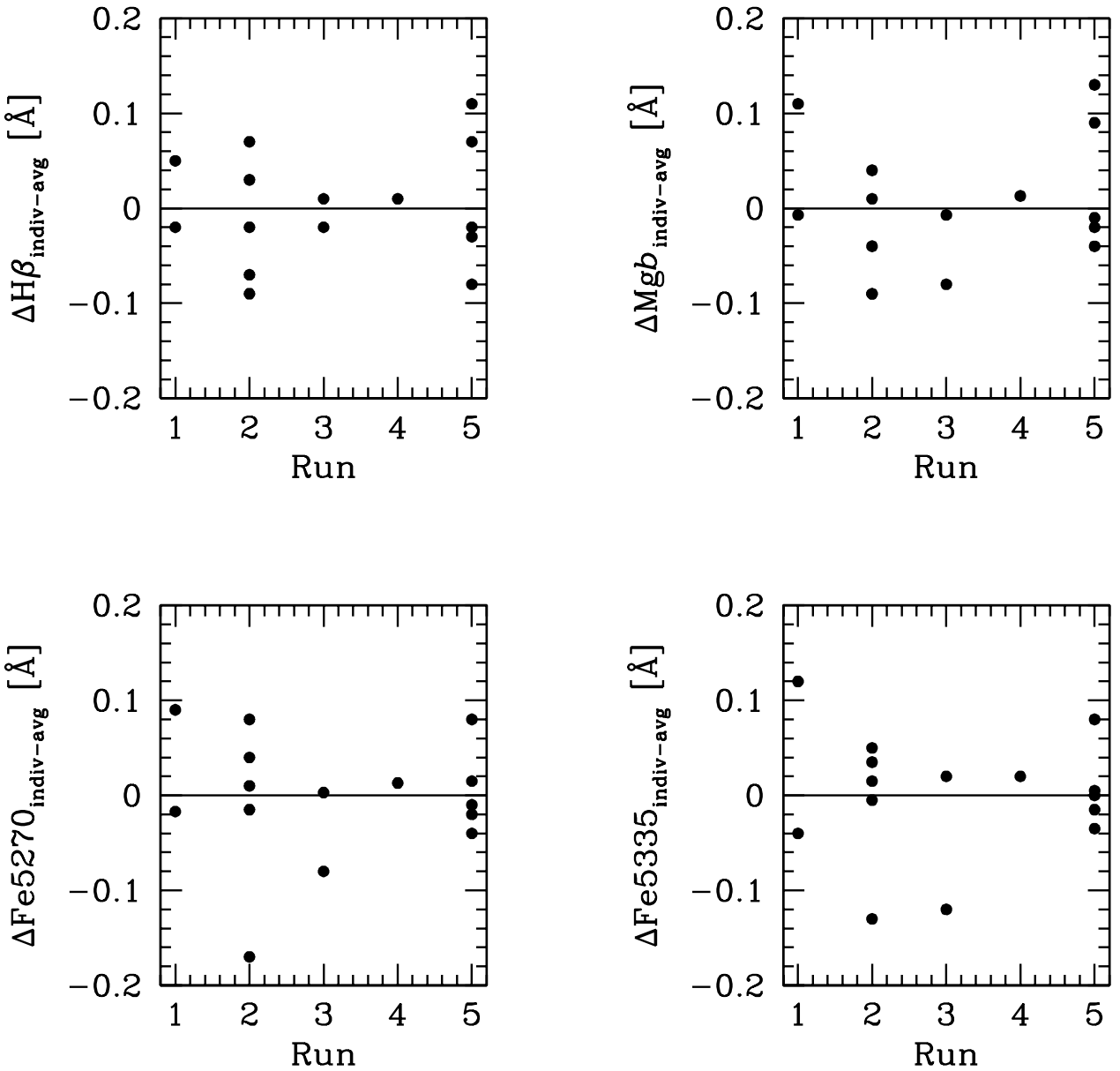


FIG. 6.— Stars which were observed repeatedly during the observing program are shown. Unlike in Figs. 4 and 5, individual index measurements are compared to the average index measurement for each star, not to the Lick/IDS system. Thus this shows the internal error in each index, independent of the uncertainty in calibrating to the Lick/IDS system.

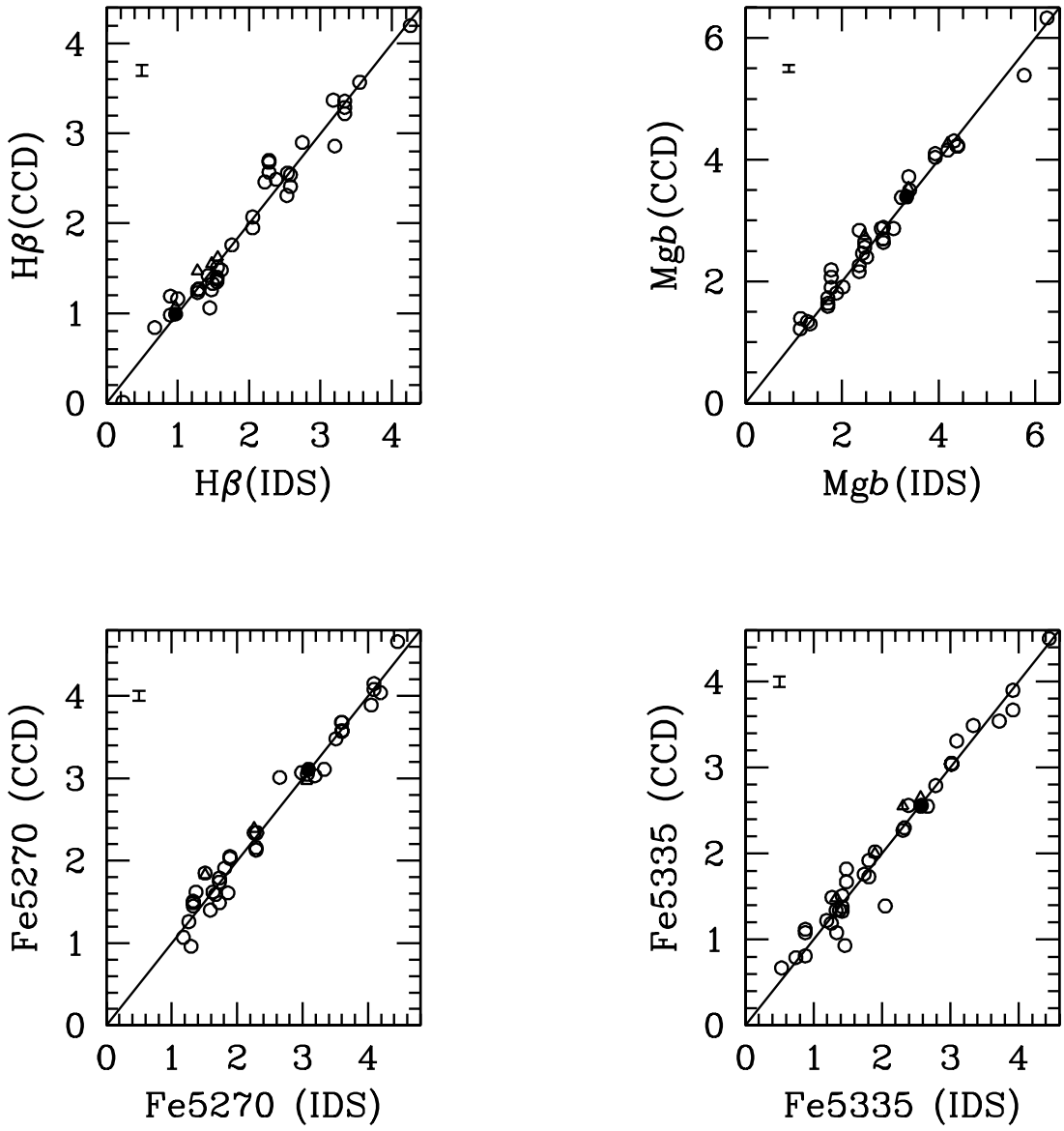


FIG. 7.— The calibrated primary index measurements for all standard stars are plotted against the standard value for that star on the Lick/IDS system. Open circles are ordinary standard stars from this work, and the solid circle as above is the Lick/IDS internal standard star HD 51440. Several stars were observed as part of both G93 and this study; the calibrated G93 measurements for those stars are shown as open triangles. The adopted calibration is in good agreement with both the Lick/IDS system and the G93 calibration.

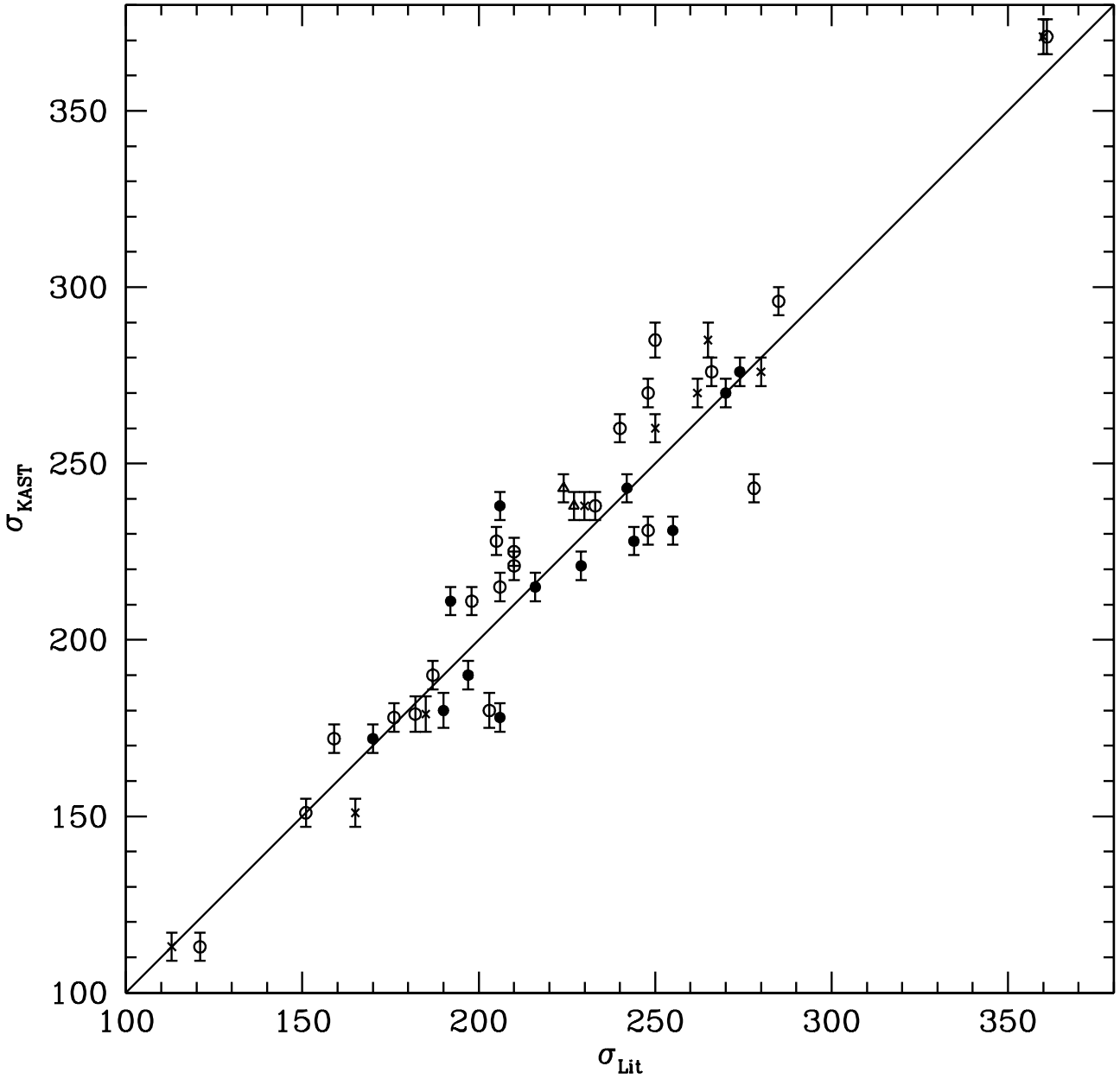


FIG. 8.— Comparisons of measured velocity dispersions between galaxies in this study and in other data sets. Open triangles are compared with G93. Black open circles, x's, and solid circles are compared with Faber et al. (1989), Faber et al. (1997), and Denicoló et al. (2005) respectively. The velocity dispersion measurements from this study are in good agreement with previous work.

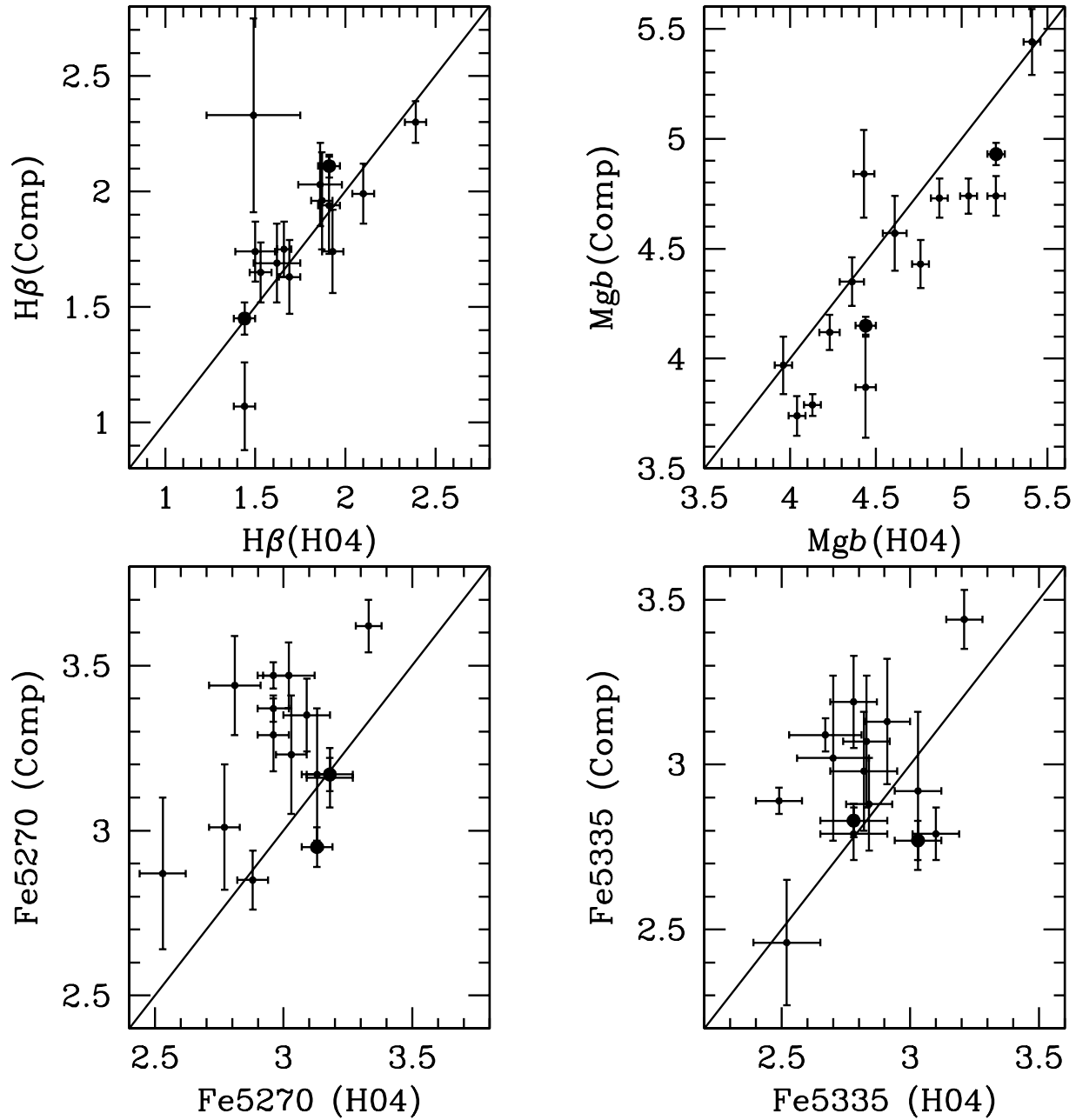


FIG. 9.— Comparisons of measured spectral indices between galaxies in this study and in other data sets. Points in large type are compared with G93. Points in small type are compared with Denicoló et al. (2005).

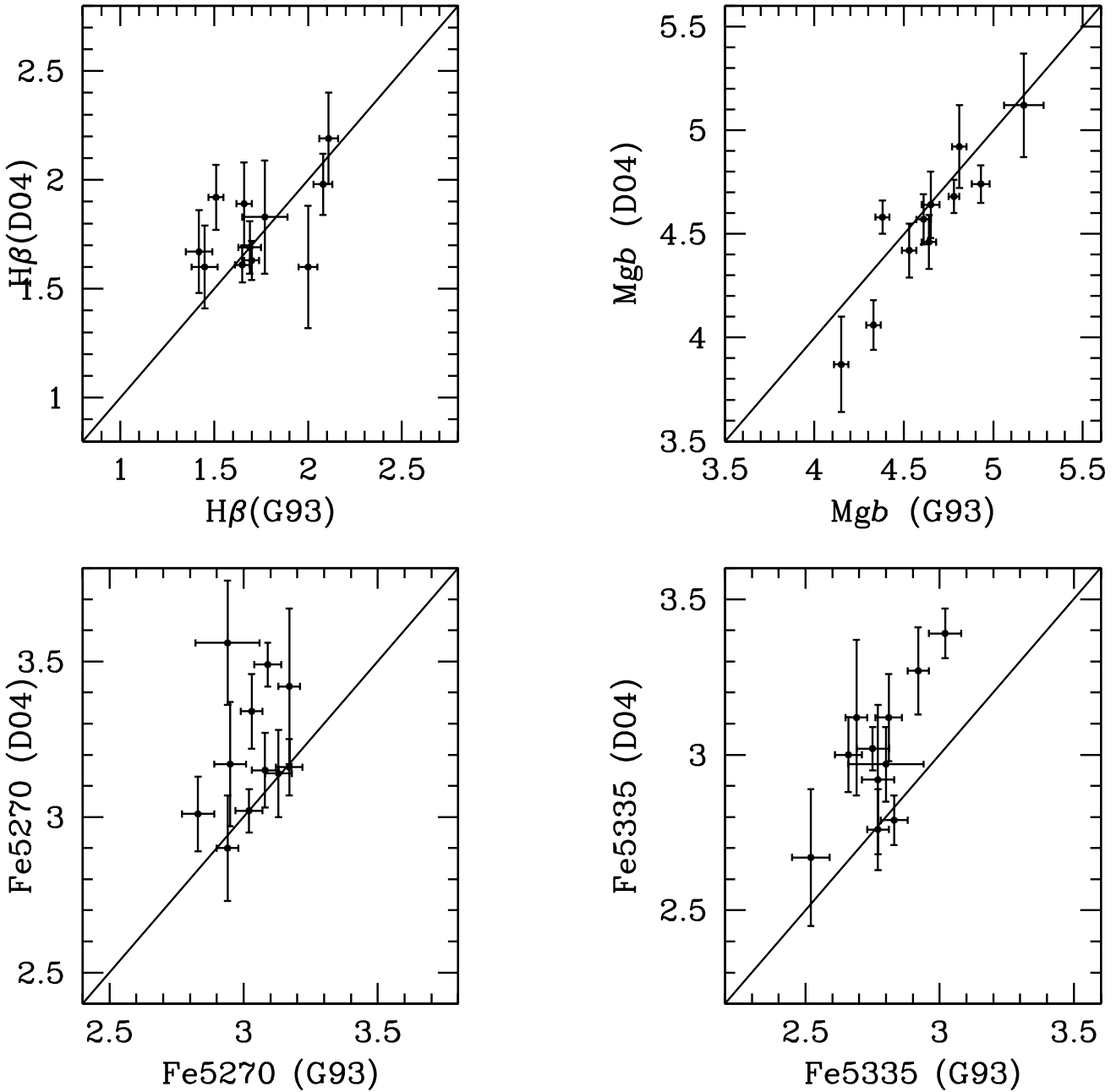


FIG. 10.— Comparisons of measured velocity dispersion and spectral indices between galaxies in G93 and in Denicoló et al. (2005). The fact that the Denicoló et al. (2005) data set deviates from the G93 in each quantity in the same way that the Denicoló et al. (2005) data set deviates from the volume-limited data set (Fig. 9) lends confidence that the volume-limited data set has been successfully calibrated onto the Lick/IDS system.

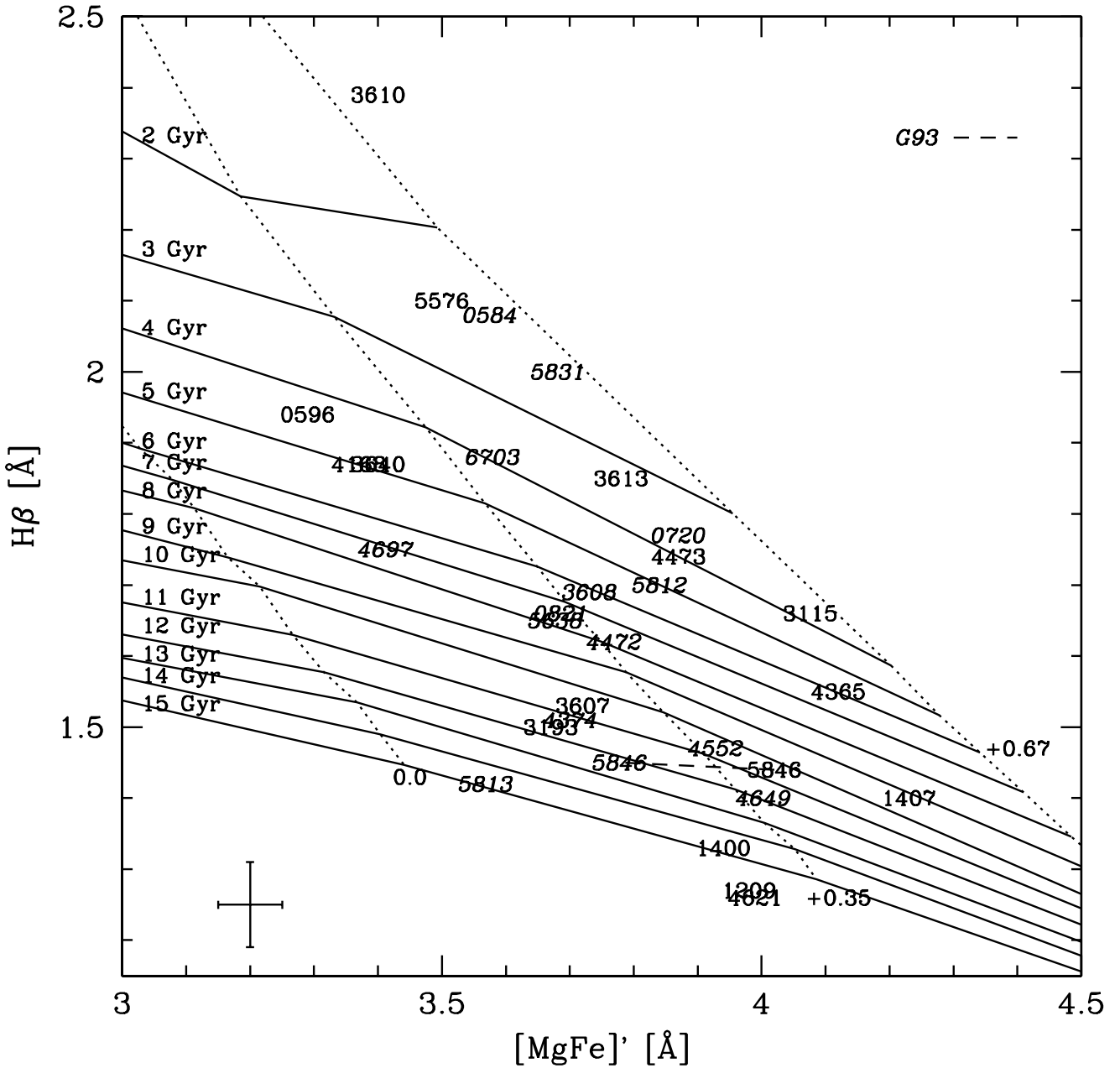


FIG. 11.— The galaxies in the volume-limited sample are plotted on age-metallicity grids from TMB. The horizontal axis is the $[\text{MgFe}]'$ index defined by TMB to be independent of $[\alpha/\text{Fe}]$. Galaxies in normal type are from this study, while galaxies in italics are members of the volume-limited sample from the G93 data set. A dashed line connects the measurements of NGC 5846 from the two data sets; this galaxy provides a direct empirical test of the accuracy of the index measurements and consistency of the Lick/IDS calibration. Although the $\text{H}\beta$ measurements are in excellent agreement between the two studies, the Mgb , Fe5270 , and Fe5335 index measurements are discrepant by more than two standard deviations. Much of this discrepancy results from the unusually large difference in measured velocity dispersion between the two studies. Typical error bars are shown in the lower left. The volume-limited sample is in agreement with previous work, showing a wide range of ages and a smaller range of supersolar metallicities.

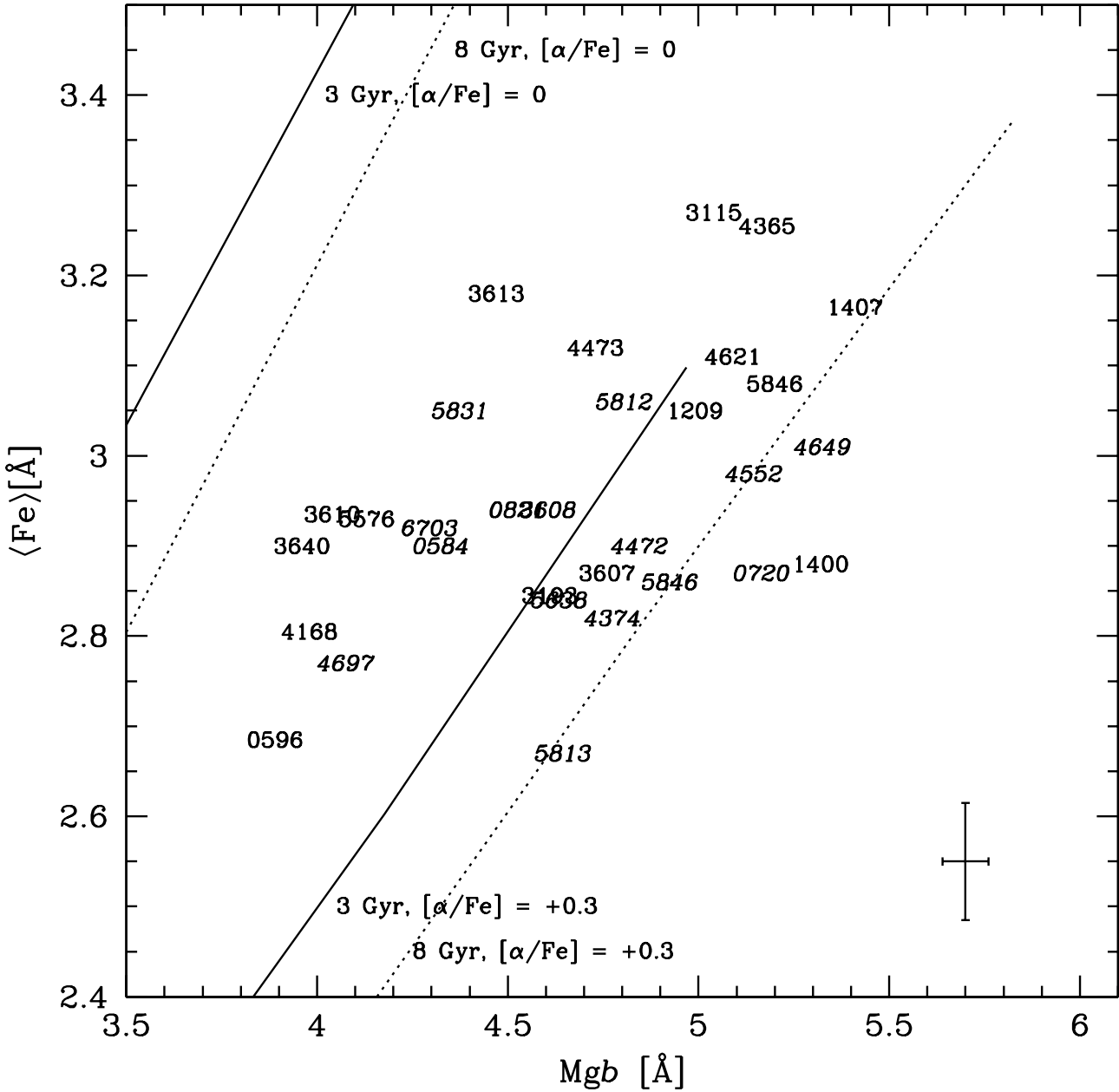


FIG. 12.— The galaxies in the volume-limited sample are plotted against iron and magnesium lines to measure $[\alpha/\text{Fe}]$. Models from TMB are shown, at 3 Gyr age (solid lines) and 8 Gyr age (dotted lines), and $[\alpha/\text{Fe}]$ values of 0.0 and +0.3 dex. Galaxies are presented as in Fig. 11. Typical error bars are shown in the lower right corner. The two sets of models shown illustrate the relatively small effect of age on $[\alpha/\text{Fe}]$ measurements.

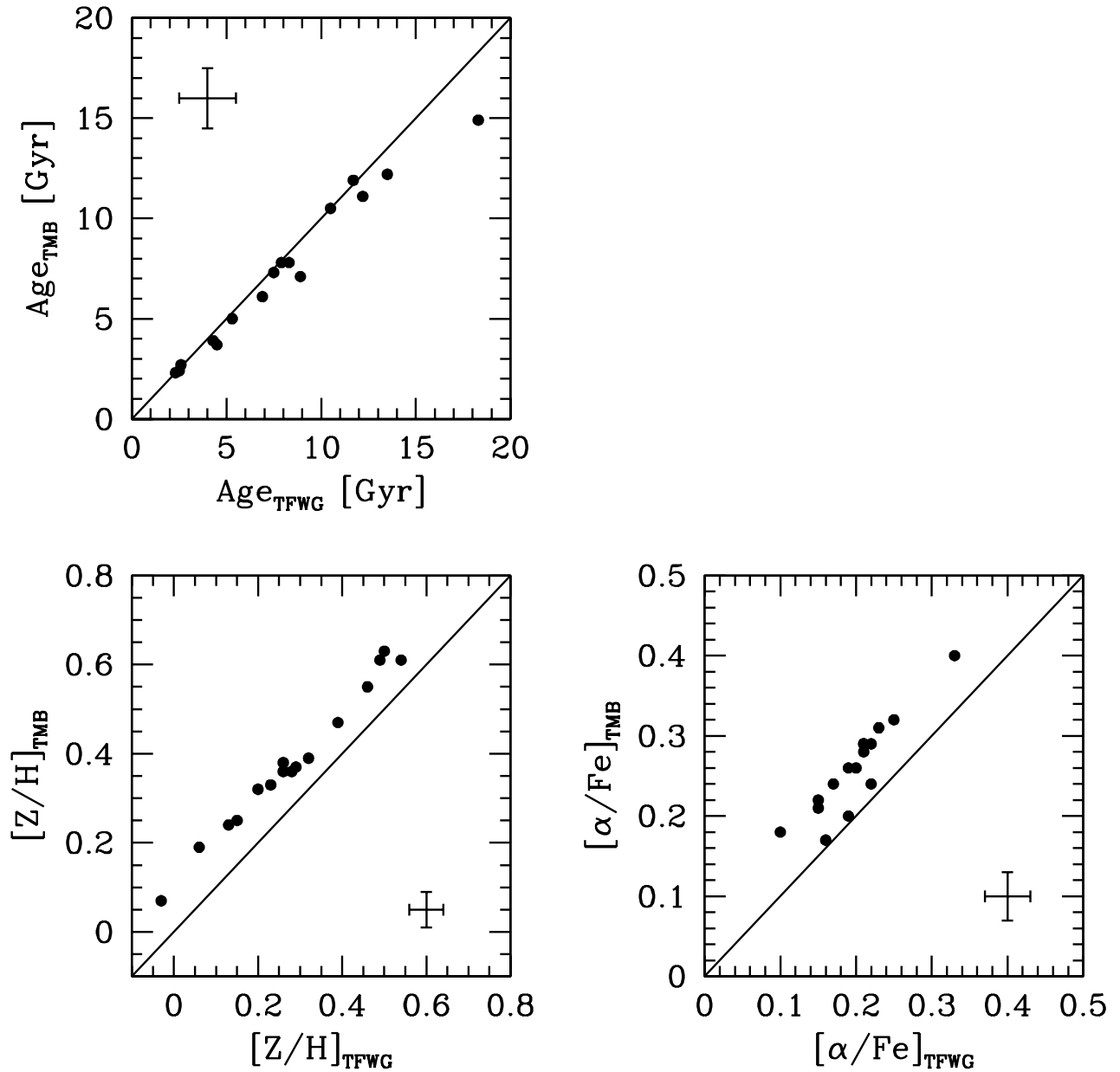


FIG. 13.— Derived physical parameters for the G93 sample are compared. Parameters from the TMB models are on the vertical axes, while parameters from Trager et al. (2000a) are on the horizontal axes. Age is compared in the upper left, metallicity in the lower left, and $[\alpha/\text{Fe}]$ in the lower right. Representative error bars are shown. The three galaxies with similar $[\alpha/\text{Fe}]$ using both models are NGC 1700, NGC 5831, and NGC 584, the three youngest galaxies plotted. The qualitative difference between the two models is negligible. TMB models result in a constant offset toward larger $[\alpha/\text{Fe}]$, which in turn results in larger $[\text{Z}/\text{H}]$.

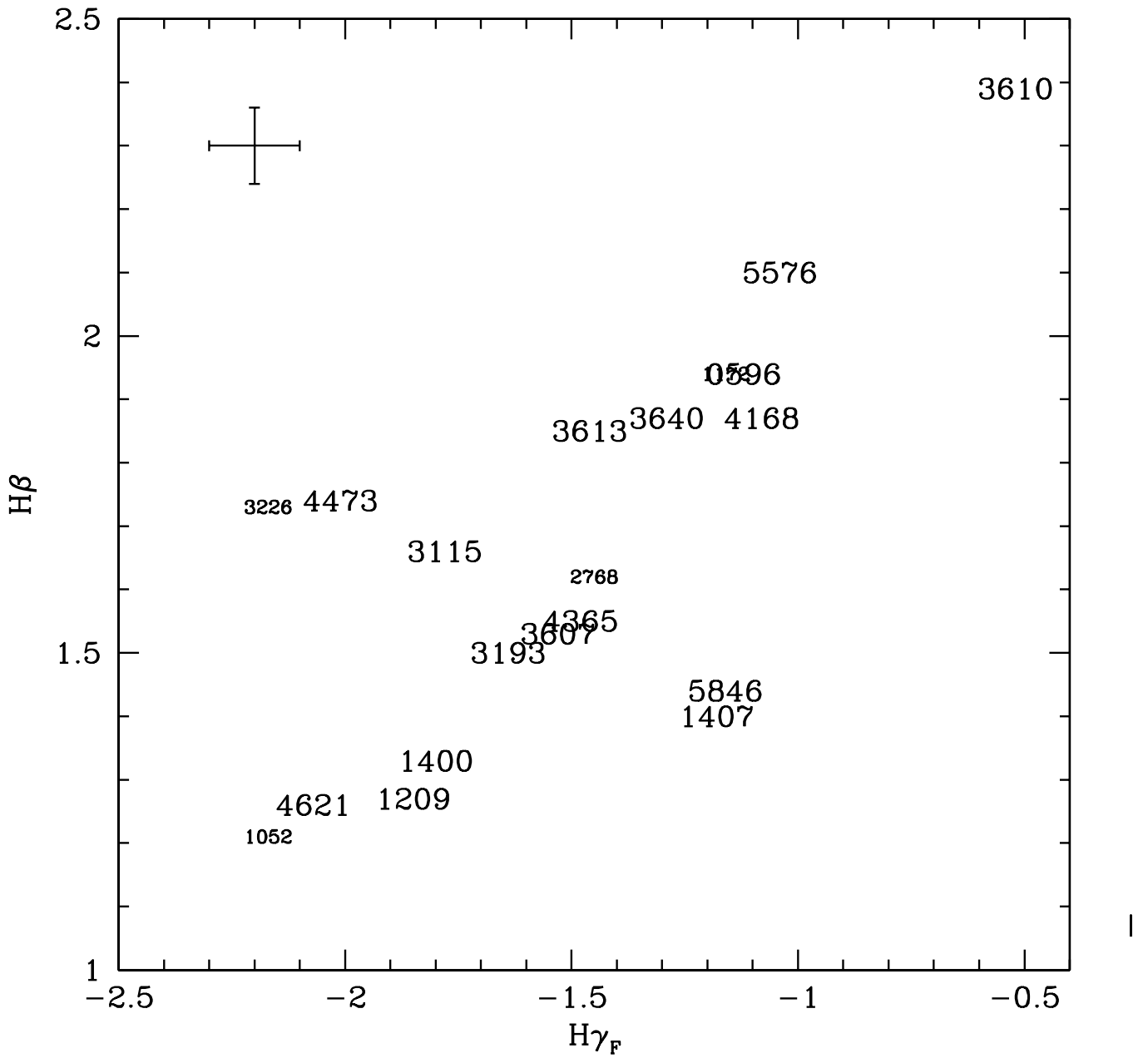


FIG. 14.— Comparison of H β and H γ_F index measurements. The galaxies in small type have large emission corrections and correspondingly large uncertainties. Typical uncertainties for the rest of the galaxy sample are presented in the upper left. With the exception of four outliers, the Balmer index measurements follow a tight linear relation.

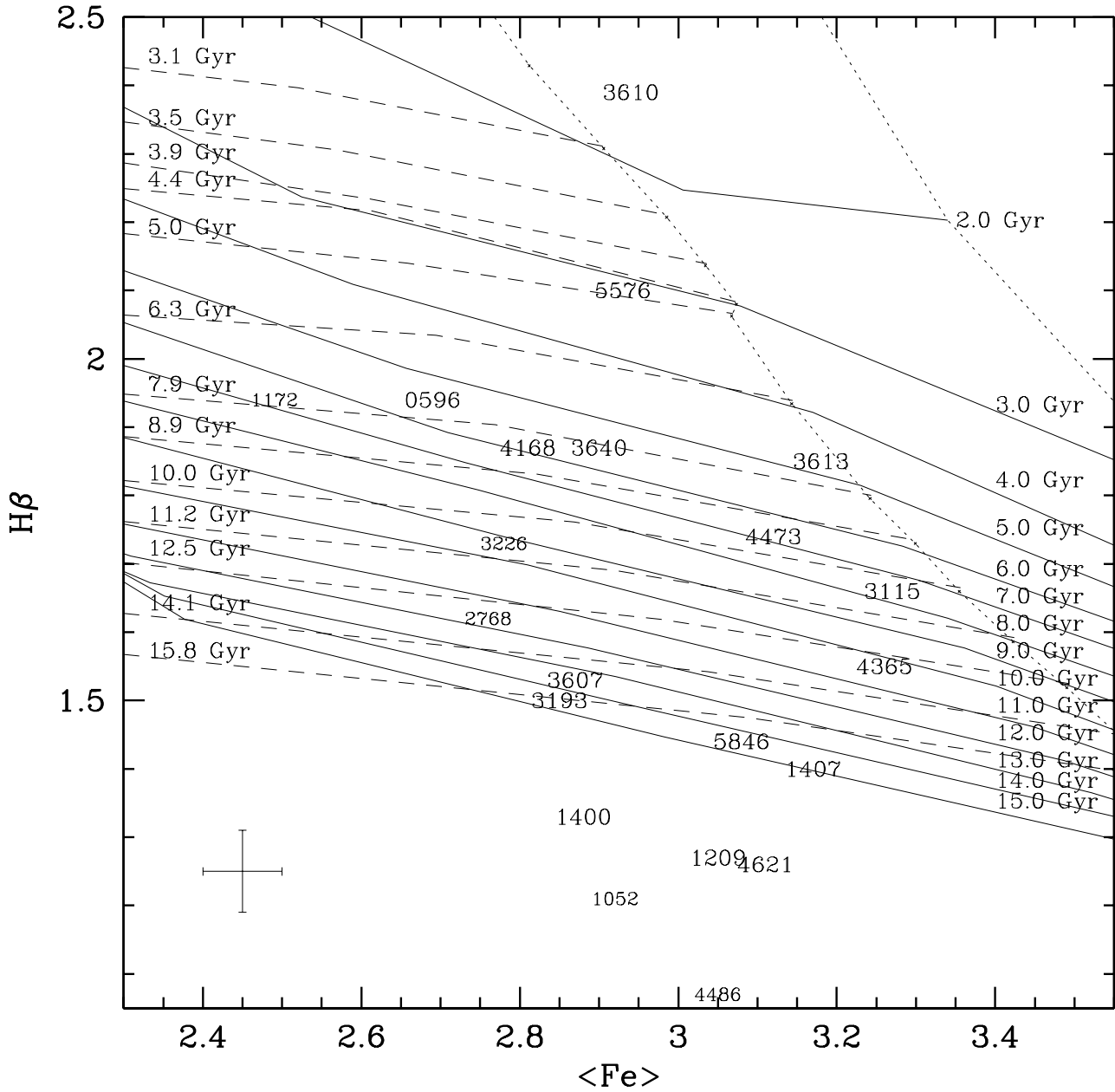


FIG. 15.— The galaxy sample from this work is plotted on the $H\beta$ vs. $\langle Fe \rangle$ plane, along with two sets of model grids. Models in solid type are from TMB with $[\alpha/Fe] = 0.0$, while models in dashed type are from Schiavon (2005). In both sets of models only the most metal-rich isometalllicity line (TMB: $[Z/H] = +0.67$; Schiavon: $[Fe/H] = +0.2$) is plotted (dotted lines). Isochrone lines for each set of models are labeled. As above, galaxies in small type have large emission corrections. Typical uncertainties for the remaining galaxies are presented in the lower left. A consistent age offset is apparent between the two sets of models, in the sense that the Schiavon models measure older ages by ~ 2 Gyr compared to the TMB models.

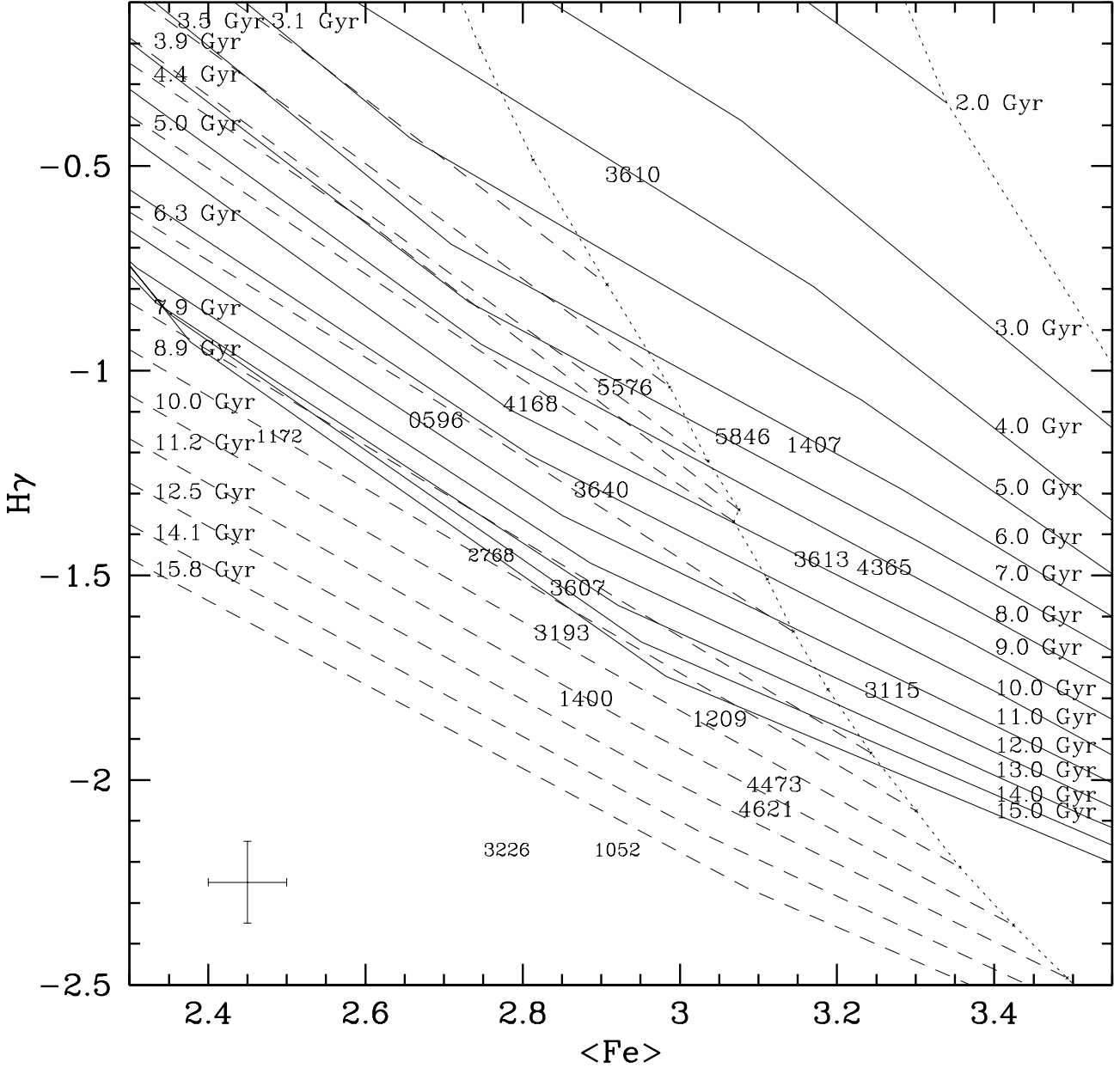


FIG. 16.— Galaxies and dashed models are as in Fig. 15. Models in solid type are from Thomas, Maraston, & Korn (2004) with $[\alpha/\text{Fe}] = 0.0$. The two sets of models are substantially different from each other in the $\text{H}\gamma_F$ vs. $\langle \text{Fe} \rangle$ plane. This is primarily due to the Thomas et al. (2004) models predicting larger $\text{H}\gamma_F$ equivalent widths by $\sim 0.4 \text{ \AA}$ compared to the Schiavon models. As a result, age measurements using the Schiavon models are younger by several Gyr compared to the Thomas et al. (2004) models.

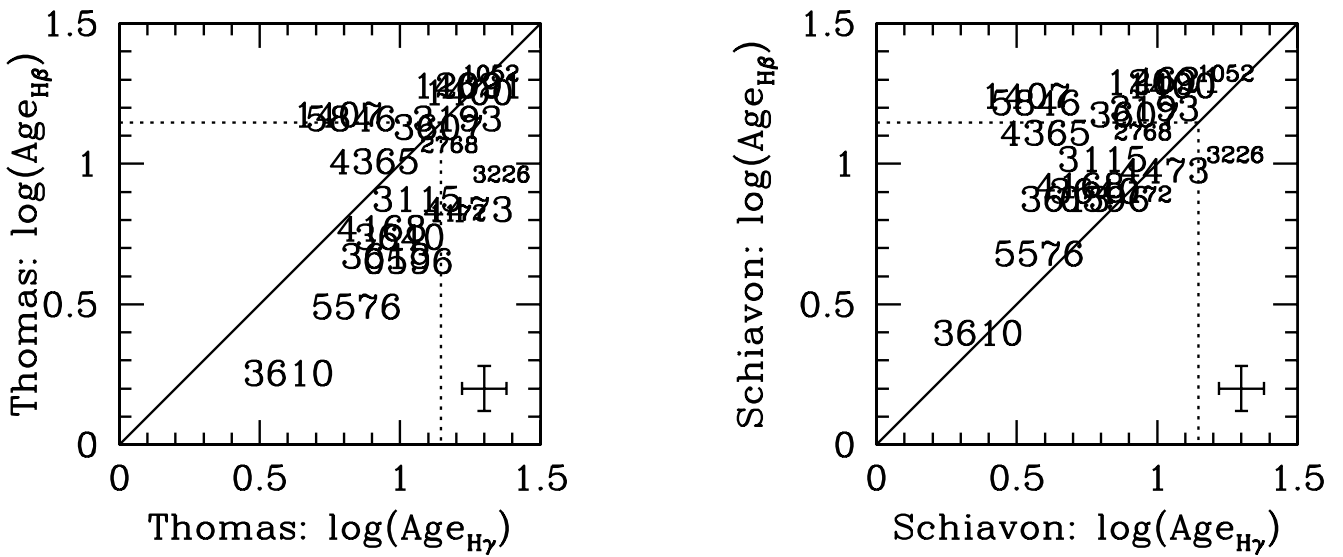


FIG. 17.— Ages derived using the model grids in Figs. 15 and 16 are compared. Measurements in the left panel are based on the Thomas et al. models, while measurements in the right panel are based on the Schiavon models. As above, galaxies in small type have large emission corrections. Typical age uncertainties for the remaining galaxies are presented in the lower right. Dotted lines are drawn at Age = 14 Gyr on each axis. The galaxies with inconsistent Balmer measurements (outliers in Fig. 14) result in discrepant ages using both sets of models. The two sets of models are in qualitative agreement, though as expected from Figs. 15 and 16 they are in systematic quantitative disagreement, typically by 2–4 Gyr. The Thomas et al. models result in older ages on the H β grids (Fig. 15) and younger ages on the H γ grids (Fig. 16). Neither set of models gives fully consistent ages between the two grids. The Schiavon models are more consistent than the Thomas et al. models at young and intermediate ages, while the Thomas et al. models are more consistent for extremely old (Age > 12 Gyr) galaxies. For the majority of galaxies, the difference between ages derived using different sets of models is significantly greater than the difference between ages derived using different Balmer indices. As a result, the conclusion is that the choice of model is more important than the choice of age-sensitive Balmer index in measuring SSP parameters.

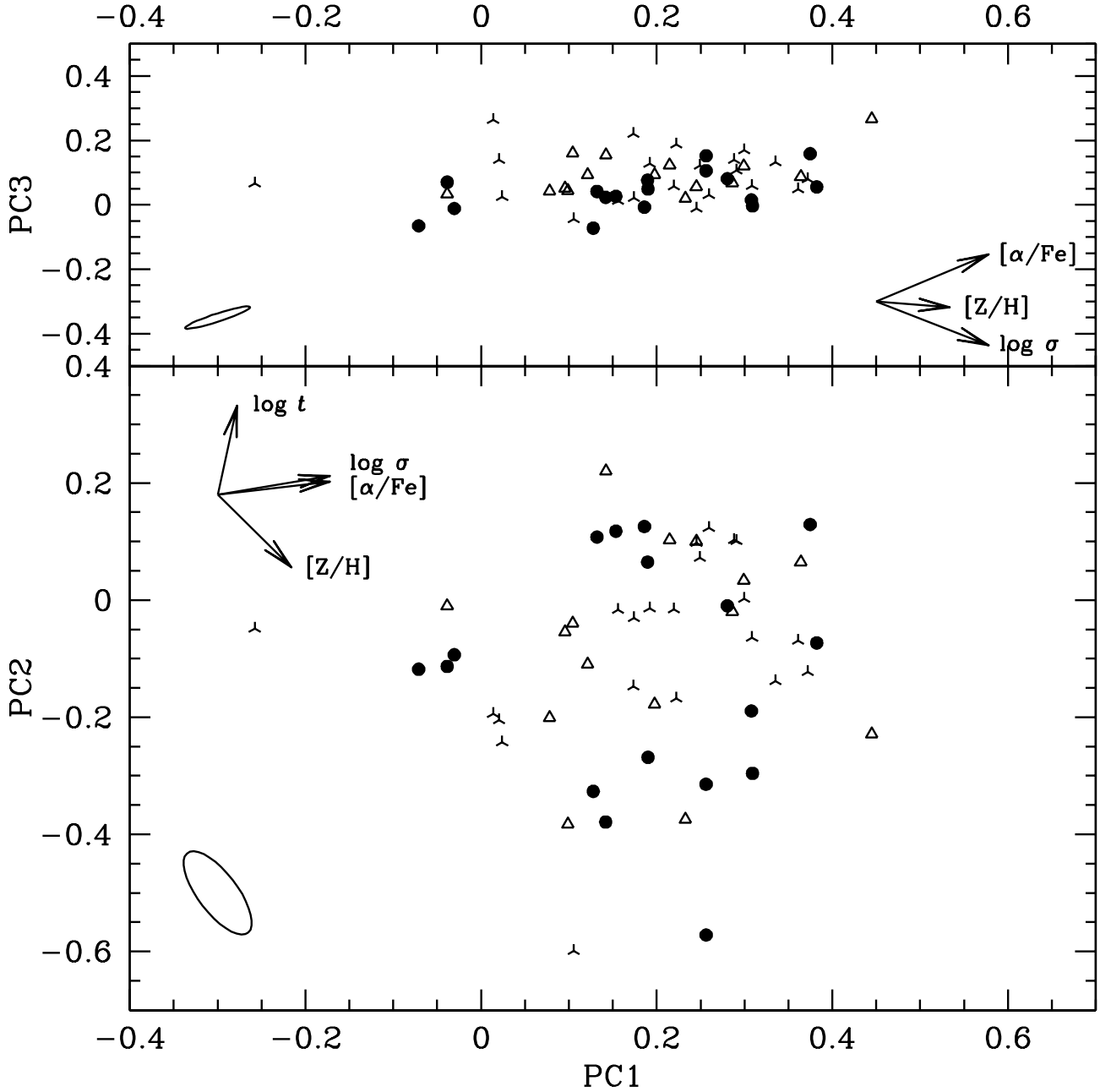


FIG. 18.— Principal component projection of the metallicity hyper-plane of TFWG. Solid circles are from this study. The remaining points are from G93; open triangles are in the volume-limited sample while skeletal symbols are not. Error ellipses are shown for the measured index and calibration errors for this study (solid ellipses). The projection of each SSP parameter in principal component space is shown. PC1 is primarily sensitive to $\log \sigma$ and $[\alpha/\text{Fe}]$, with some metallicity sensitivity. PC2 is sensitive to age and metallicity, while PC3 is dependent on both $\log \sigma$ and $[\alpha/\text{Fe}]$. Conceptually, one can think of PC1 measuring a galaxy's position along the $\text{Mg}-\sigma$ relation, PC2 measuring position along an age–metallicity relation, and PC3 measuring deviations from the $\text{Mg}-\sigma$ relation. The volume-limited and G93 samples are consistent with being drawn from the same distributions in each principal component axis.

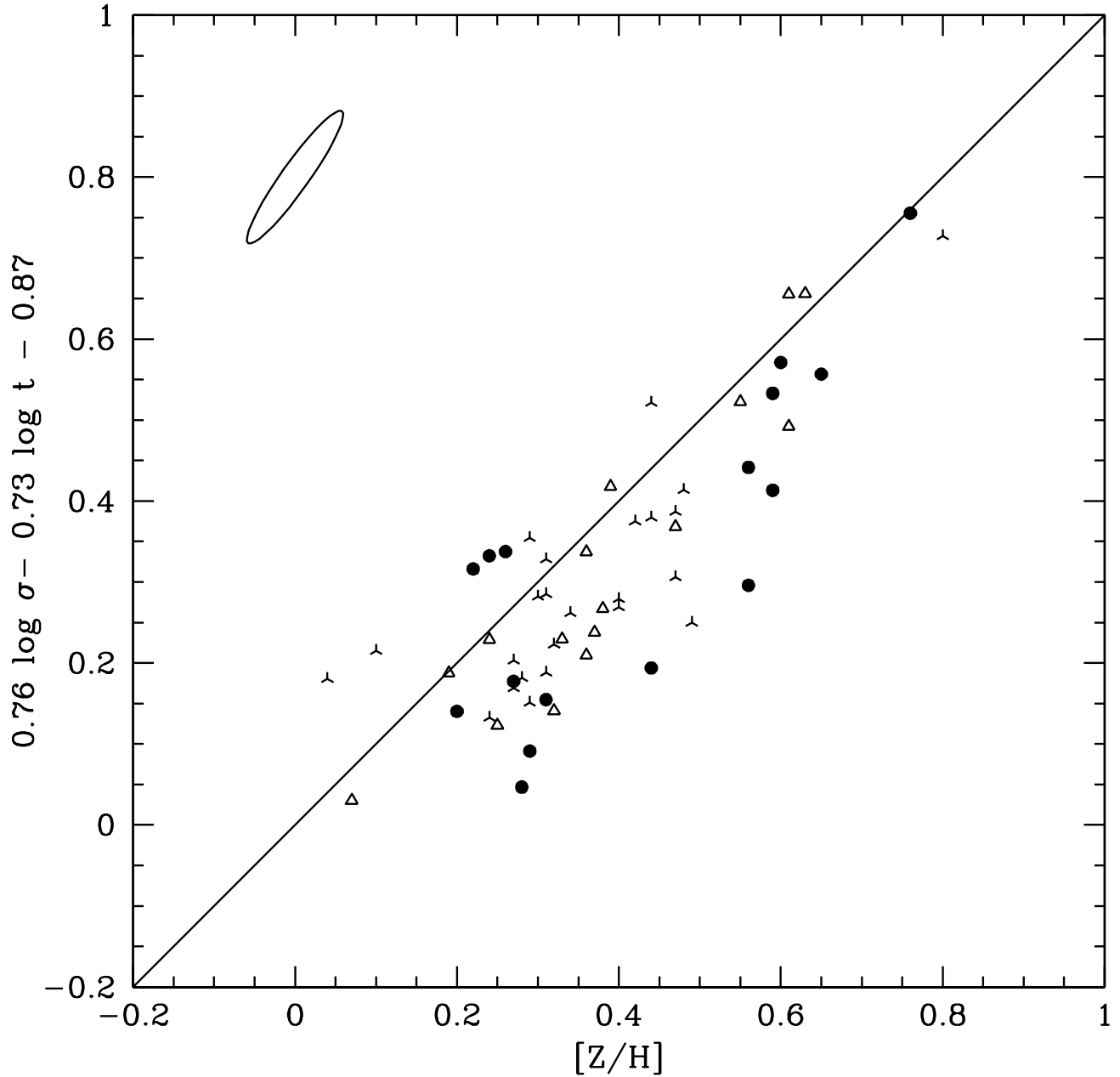


FIG. 19.— The Z -plane as defined in TFWG (solid line). Points are as in Fig 18. A typical 1σ error ellipse is shown in the upper left. The normalization of this relation between velocity dispersion, age, and metallicity depends on the models used, as would be expected based on Fig. 13. The difference in models readily explains the offset between the TFWG fit and the data. The most metal-rich galaxy is NGC 3610, which is examined in detail in Howell et al. (2004). The volume-limited and G93 samples are consistent with being drawn from the same distribution along this edge-on projection of the Z -plane.

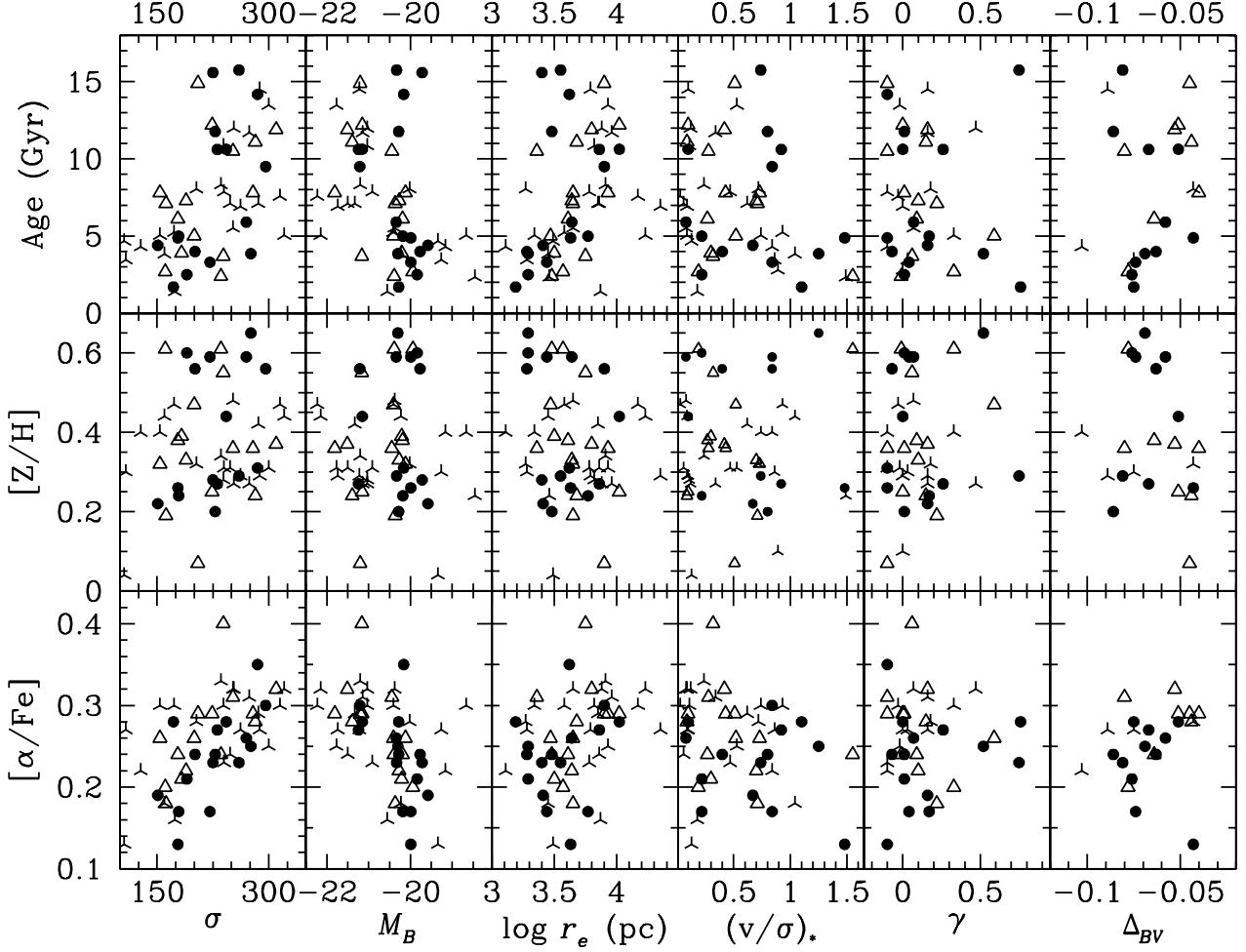


FIG. 20.— Comparison between parameters relating to the average stellar composition (age, $[Z/H]$, $[\alpha/\text{Fe}]$) and parameters relating to galaxy size (σ , M_B , $\log r_e$), shape $((v/\sigma)_*)$, density profile (the power-law slope γ), and color gradient. Points are as in Fig 18. Several well-known trends are apparent. The $[\alpha/\text{Fe}]$ – σ relation is directly analogous to the Mg– σ relation (Fig. 1). It is also clear that the faintest and least massive galaxies are all relatively young, while brighter and more massive galaxies span a wide range of ages.

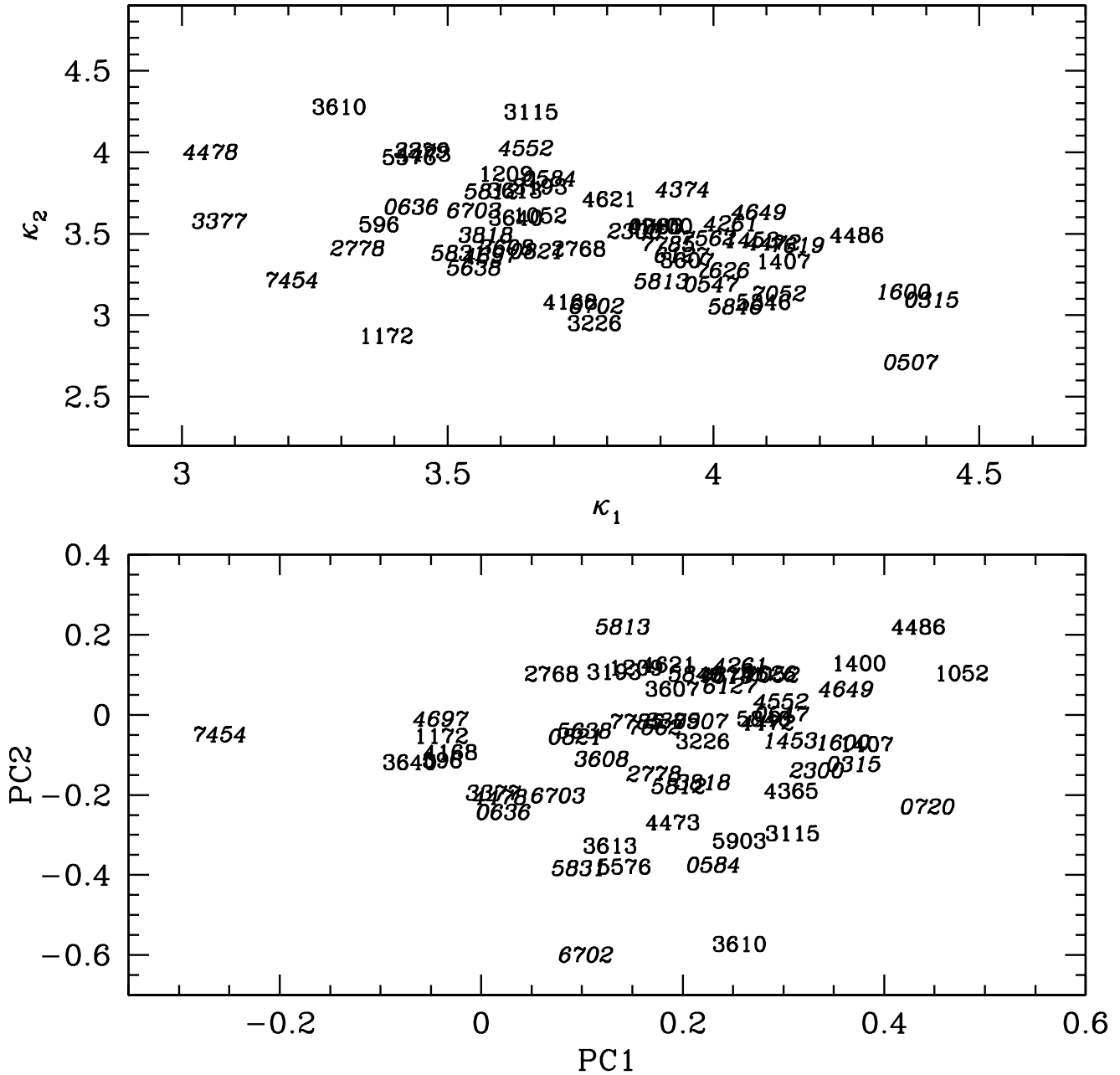


FIG. 21.— The face-on projections of the Fundamental Plane (top panel) and Z -plane (bottom panel) are shown. Galaxies in normal type are from this work, while those from G93 are in italic type. No mapping from one plane to the other is found.